Title

Assimilating observations to simulate marine layer stratocumulus for solar forecasting

Authors

Sahu, Dipak K
Yang, Handa
Kleissl, Jan

Publication Date

2018-03-01

DOI

10.1016/j.solener.2018.01.006

Peer reviewed

Assimilating observations to simulate marine layer stratocumulus for solar forecasting

Dipak K. Sahu[a], Handa Yang[a,] Jan Kleissl[a]

[a] Center for Renewable Resource Integration, Center for Energy Research, University of California San Diego,

9500 Gilman Dr., La Jolla, CA 92093, USA

Corresponding Author:

Dipak K. Sahu

Department of Earth, Ocean, and Atmospheric Science

Florida State University

1017 Academic Way

430 LOVE Building

Tallahassee, FL-32306

Email: dsahu@fsu.edu

Phone: 8587661203

Present Address:

Dipak K. Sahu

Department of Earth, Ocean, and Atmospheric Science

Florida State University

1017 Academic Way

430 LOVE Building

Tallahassee, FL-32306

Email: dsahu@fsu.edu

Abstract -- Integration of solar energy forecasts into the electric network is becoming essential because of the continually increasing penetration level of solar energy. Three-dimensional numerical weather prediction (NWP) models predict the weather based on the current weather conditions (called initialization) and simulate the ensuing atmospheric processes. The accuracy of forecasts therefore depends, in part, on the accuracy of the model initializations. Data assimilation is recognized as the most widely used technique to improve the initialization into NWP models. In this study, meteorological observations from the surface and upper-air in-situ networks over the southern California coast are assimilated into the advanced research version of the Weather Research and Forecasting (WRF) model using a three dimensional variational data assimilation technique (3DVAR). A single observation test was conducted to tune-up the length scale and variance scale along with the regional domain-dependent background error statistics. A customized version of 3DVAR data assimilation was deployed with two sets of cyclic data assimilation with 6-h and 1-h assimilation windows along with the cold-start mode. The cyclic data assimilation experiments consistently outperformed the cold-start data assimilation and WRF for intra-day Global Horizontal Irradiance (GHI) and Clear Sky Index (CSI) forecast. Hourly cyclic assimilation showed the highest forecast skill score against ground measurements and satellite measurements. Even at the coastal stations with more challenging meteorological conditions, the hourly cyclic assimilation consistently outperformed the 24-h persistence forecast. The average (mean of four case studies) hourly cyclic data assimilation showed the highest forecast skill score in GHI and CSI intra-day forecast with reference to 24-h persistence forecast up to 39.4% and 40.7% respectively at the coastal stations. The spatial distributions of GHI biases estimated against SolarAnywhere satellite measurements showed that the hourly cyclic assimilation consistently improved the stratocumulus cloud coverage, thickness, and life time over the coastal region, but biases are still present further inland.

Keywords:
Solar energy forecasting, marine layer stratocumulus cloud, NWP, intra-day forecast, data assimilation

1. Introduction

The increasing contribution of solar energy to electric power generation motivates accurate forecasts of solar irradiance at the earth's surface. Satellite-based solar irradiance forecasts, sky-imager based solar irradiance forecasts, and statistical forecasts are considered to be the most accurate solar irradiance forecasts for horizons up to 6 h. However, these forecast methods become inferior beyond 6 h ahead. Generally, grid operators aspire to receive forecasts of solar energy for at least a day ahead. State-of-the-art numerical weather prediction (NWP) models can provide improved solar irradiance forecasts for a day ahead period.

Solar irradiance depends on both geographical location and meteorological conditions. The major concern in solar power generation is high variability in the amount of incident solar irradiance due to the presence of clouds. Accurate cloud forecasting within a NWP model is challenging due to the complex multiscale physical processes that influence cloud formation. Forecasting the low clouds in the marine layer over coastal southern California is especially challenging. Marine layer clouds are typically shallow and exist near the inversion of the planetary boundary layer (PBL). Recently, several studies have been conducted to understand the physical processes associated with the formation of marine layer clouds and their representation within NWP models (Ghonima et al., 2017; Kazil et al., 2016; Ghonima et al., 2016; Sandu et al., 2009; Hu et al., 2010; Jankov et al., 2011).

Most operational meteorological centers use NWP models to forecast solar irradiance, although they are known to over predict solar irradiance. Mathiesen and Kleissl (2011) found the mean bias error (MBE) and root mean square error (RMSE) of hourly averaged surface irradiance forecast exceeded 30 W m^{-2} and 110 W m^{-2}, respectively, over southern California. Similarly, the multi-model inter-comparison study conducted by Perez et al. (2013) found noticeably positive MBE over the United States. A similar study conducted by Lara-Fanego et al. (2012) over southern Spain found for forecasts with a 24-h lead time that the MBE of forecasted global horizontal irradiance (GHI) was 2% for clear sky conditions and 18% for cloudy conditions. The RMSE of forecasted GHI ranged from 10% under clear sky to 50% for cloudy conditions.

Three-dimensional NWP models predict future weather conditions based on the current weather conditions (called initial conditions) and physical parameterizations to simulate ensuing atmospheric processes. The accuracy of forecasts therefore depends, in part, on the accuracy of the model initializations (Kalnay, 2003). Initialization describes the process of determining the

initial state of the atmosphere in terms of various meteorological parameters. Data assimilation is recognized as the most widely used technique to improve the initialization into NWP models.

In the past few decades, the advancement of computational resources, novel data assimilation algorithms and new observation networks including remote sensing and in-situ observations has continually improved the model initialization (or analysis) and subsequent forecasts. Despite the advancements in data assimilation and computational facilities, the use of in-situ observations, especially surface observations, remains a challenging problem. In addition, due to heterogeneous topography, considerable difficulties have been encountered when assimilating surface observations over complex terrain. Currently, only a limited number of surface observations are used in NWP. In the National Centers for Environmental Prediction/National Center for Atmospheric Research (NCEP/NCAR) 50-year reanalysis (Kalnay et al., 1996), only surface pressure observations were assimilated.

Since NWP models still have significant biases in GHI forecast over different parts of the globe, and forecast accuracy significantly depends on model initialization, in this study we attempted to improve the model initialization by assimilating in-situ observations. The in-situ observations from near-surface and radiosonde networks contain a wealth of information about the lower atmosphere. Notably, near-surface observations are available at high temporal resolutions and dense spatial coverages, compared to the other sources of upper-air or remote sensing observations. However, several recent studies (Sahu et al., 2016; Dash et al., 2013; Hacker et al., 2007; Stensrud et al., 2009; Pu et al., 2013; Reen and Stauffer, 2010) showed significant improvements in short-range forecasts by assimilating near surface observations within a mesoscale NWP model. In this study, three-dimensional variational (3DVAR) data assimilation (Barker et al., 2004) is used within the Weather Research and Forecast (WRF) modelling framework WRF V3.6.1 (Skamarock et al., 2008) to improve the model initialization by assimilating the in-situ observations (temperature, dew point temperature, wind speed, wind direction and surface pressure) from the surface and radiosonde networks over the southern Californian coast. The purpose of this study is to examine the impact of assimilation of near-surface and radiosonde observations on the improvement of an intra-day GHI forecast. The initial and boundary conditions for the model simulation are derived from the North American Mesoscale model (NAM) 6-h analysis. The NAM data assimilation system assimilates most of the in-situ and remote sensing observations over United States to generate the 6-h analysis.

Hence, in addition to the first objective, an hourly cyclic data assimilation is also carried out along with the six-hourly cyclic data assimilation for inter-comparison of the model simulations.

The following sections are organized as follows. Detailed descriptions of the experimental design including the WRF and 3DVAR models and marine layer events are given in Section 2. The sensitivity of the tuning parameters such as length scale, variance scale, and background error statistics (BES) on the analysis increment and model forecast are analyzed in Section 3. The validation of the model simulations for liquid water content (LWC), global horizontal irradiance (GHI) and other meteorological parameters are described in Section 4. Finally, conclusions are provided in Section 5.

2. WRF model and Data assimilation technique

2.1 WRF model configuration

The WRF version 3.6.1 model (Skamarock et al., 2008) is configured with two nested domains with horizontal resolutions of 8.1 km and 2.7 km, respectively. The inner domain is centered over the southern Californian coast (as shown in Fig. 1), which is subject to marine layer stratocumulus clouds during the summer months. The total atmospheric column within the model is divided into 75 terrain-following vertical σ-levels, and 50 levels are below 3 km altitude. The model initial and boundary conditions were derived from the 0000 UTC NAM data. Here the 0000 UTC NAM data is used for model initialization instead of the most recent 0600 UTC NAM, because it delivers lower mean absolute errors (MAE) for forecasted GHI. The physics parameterizations used for this study include Morrison 2-moment microphysics scheme (Morrison et al., 2009), Goddard scheme for shortwave and longwave radiation parameterization (Chou and Suarez, 1994), Kain-Fritsch New Eta scheme for cumulus parameterization (Kain, 2004), unified Noah land surface model (Chen and Dudhia, 2001), and MYNN 2.5 scheme (Nakanishi and Niino, 2006) for the planetary boundary layer. The cumulus parameterization was used only for domain-1 (8.1 km), and it was off for domain-2 (2.7 km). The model was run for 6 h from 0600 UTC to 1200 UTC in spin-up mode, and then from 1200 UTC onward in forecast mode up to 18 h (until after sunset on the forecast day). Mesoscale models need spin-up to establish an equilibrium between moisture, temperature and the wind field before entering a forecast mode.

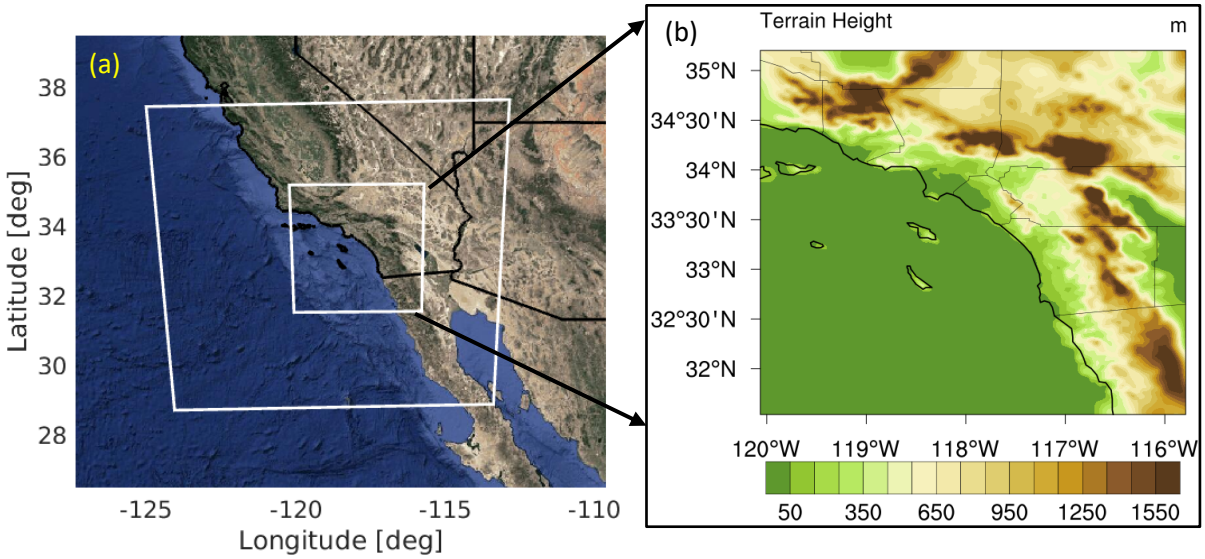

Figure 1: (a) Map of the two-nested domains used in the numerical model and (b) The terrain height (m) of the inner domain centered over southern California. Outer and inner domains are at 8.1 km (131x121x75 grid points) and 2.7 km (151x151x75 grid points) horizontal resolutions, respectively. Satellite image ©2015 Google.

2.2 3DVAR data assimilation

Three-dimensional variational (3DVAR) data assimilation uses observations from various sources and combines them with the short-range model forecast (i.e. background), which can be obtained from the WRF simulation in order to provide the accurate state of the atmosphere at model initialization (i.e. analysis). In this study, the background is a 6-h model forecast obtained from our own WRF simulations (without data assimilation). The meteorological observations assimilated in 3DVAR data assimilation are collected from surface observations, ships, and radiosonde networks as shown in Fig. 2. In addition to observations and background, background error statistics (BES) also play a major role in 3DVAR data assimilation. In variational data assimilation, BES are crucial for the quality of the analysis, because they determine to what extent the background field will be corrected to match the observations. In general, variational systems can be categorized as those data assimilation systems which provide an analysis "x_a", via minimization of the prescribed cost function $J(x)$, iteratively (Courtier et. al. 1994).

$$J(x) = J_b(x) + J_o(x) = \frac{1}{2}\left(x - x_b\right)^T \mathrm{B}^{-1}\left(x - x_b\right) + \frac{1}{2}\left[y_o - H(x)\right]^T \mathrm{R}^{-1}\left[y_o - H(x)\right] \qquad (1)$$

In eq. (1), J_b and J_o are respectively the background and observation terms of the cost function. In the above equation, the analysis $x = x_a$ represents *a posteriori* maximum likelihood (minimum

variance) estimate of the true state of the atmosphere given two sets of data, the background (previous forecast) $\boldsymbol{x_b}$ and observations $\boldsymbol{y_o}$ (Lorenc, 1986). Here, in eq. (1), "*T*" denotes the transpose operator for respective matrices. The analysis fit to these data is weighted by estimates of their errors: ***B*** and ***R*** are the background and observational error covariance matrices, respectively. The sources of observational errors are the combination of instrumental and representativeness errors. The representativeness error is an estimate of inaccuracies introduced in the observation operator ***H*** (linear or nonlinear) used to transform the model grid point analysis ***x*** to observation space ***H(x)***. This representativeness error is resolution dependent and may also include a contribution from approximations in ***H***.

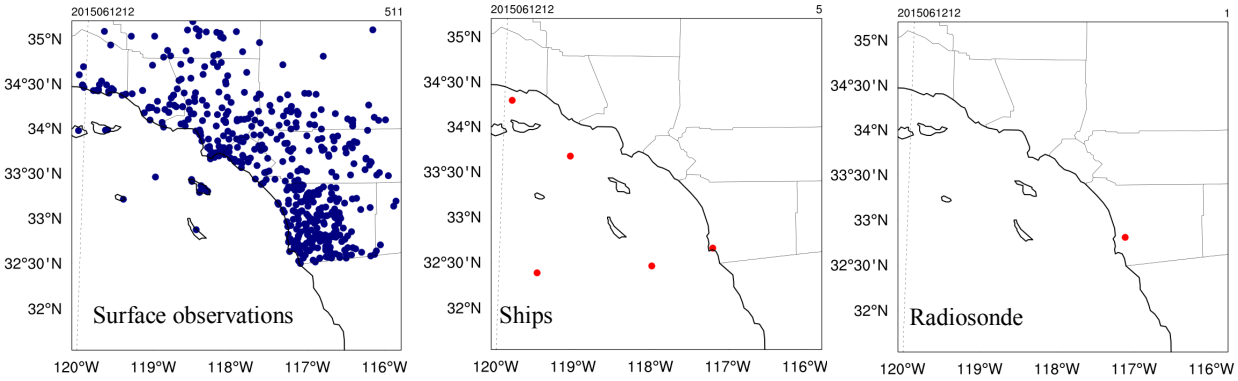

Figure 2: Distributions of conventional in-situ observations collected from surface observations (left), ships (center) and radiosonde networks (right). Blue and red dots show the location of the observations within the domain-2.

2.3 Background error statistics (BES):

The WRF 3DVAR system is developed based on a multivariate incremental formulation (Courtier et al., 1994). The background error (BE) covariance matrix plays an important role in variational data assimilation system by (i) weighting the *a priori* state (background) obtained from a previous short forecast (in this case, 6-h forecast), (ii) smoothing and spreading meteorological information from observation points to model grids, and (iii) by imposing an equilibrium between the model control variables (Daley, 1991; Bannister, 2008a, b). In WRF 3DVAR modeling system, users can choose to estimate the BE covariance matrix (***B***), rather than using the default BES provided by NCEP/NCAR to achieve consistency between BES and the forecast model resolution. In reality, the BE matrix may be dependent on the synoptic

conditions (Barker et al., 2004). Sahu et al. (2014) and Wang et al. (2014) found significant improvement in the model simulations by estimating the domain-dependent BE matrix. Wang et al. (2014) found that BE variances vary from month to month as well as diurnally in the low level atmosphere.

The commonly used National Meteorological Center (NMC: now named the National Centers for Environmental Prediction) method (Parrish and Derber, 1992) is employed to estimate the BE matrix (*B*: eq. (2)) for this study. The NMC method provides a climatological estimate of the BE matrix by considering the average forecast differences between forecasts of different lengths, but valid at the same time for a month or longer. The short-range forecast differences are considered between 24-h and 12-h forecasts valid at the same time for the months of June and July (marine layer cloud months):

$$B = \overline{(x_b - x_t)(x_b - x_t)^T} = \overline{\varepsilon_b \varepsilon_b^T} \approx \overline{(x_f^{T+24} - x_f^{T+12})(x_f^{T+24} - x_f^{T+12})^T}, \quad (2)$$

where x_t is the true atmospheric state, x_b is the background (i.e., first-guess), $\boldsymbol{\varepsilon_b}$ is the background error, $\boldsymbol{x_f^{T+24}}$ and $\boldsymbol{x_f^{T+12}}$ are 24- and 12-h forecasts respectively from the WRF model simulations over domain 2, valid at the same time. The overbar denotes an average over time and "*T*" denotes the transpose operator.

2.4. Single observation test

For the operational NWP models, performing optimum interpolation or least squares curve fitting of the observations into regular grids is insufficient because not enough data are available to initialize the current models. This is because the number of degrees of freedom in the high resolution NWP model is of the order of 10^7, whereas the total number of conventional observations of the variables used in the NWP model (e.g., from radiosondes and synoptic observations) is of the order of 10^4 (Kalnay, 2003). For this reason, it became clear that, in addition to the observations, it was necessary to have a complete first guess estimate of the state of the atmosphere at all grid points in order to generate the initial conditions for the forecasts (Bergthorsson and Doos, 1955). The first-guess is also known as the background field from a short range forecast. In recent years much effort has been spent in the development of variational data assimilation to replace optimum interpolation and least squares method. Advantages of the variational approach include (a) the ability to assimilate new types of observed quantities,

including remotely sensed data such as satellite and radar observations (e.g. radiances and Doppler wind), as they do not directly measure the observations used in the NWP models (wind, temperature, moisture and surface pressure) and (b) the imposition of dynamic balance either implicitly through the inclusion of the forecast model itself (four-dimensional variational data assimilation (4DVAR)) or explicitly through the use of balance equations (3DVAR).

The BE covariance matrix determines the respective weights given to each observation to generate the analysis. However, the accurate estimation of BE statistics is a major challenge in the 3DVAR data assimilation system. The horizontal and vertical structure of the correlation function is especially important and determines the optimal use of observed information in analysis and its horizontal propagation within the study domain. Typically, when the BE structure is dominated by large scales, the correlation functions are relatively wide. This implies that small scale observed details tend to be filtered out in the analysis step, and that point observations are propagated over large spatial distances (Daley, 1991). Diagnostics of the length-scale of BE correlation functions are often used as an approximate indicator of the degree of spatial smoothing. Following the classical definition of a differential length-scale by Daley (1991), the length-scale diagnosis describes the curvature of the correlation functions near their origin. Thus, the smaller the length-scale is, the faster the correlation decreases with distance.

The sensitivity of variance scale for each control variable within the BE matrix is analyzed here by considering a pseudo single observation test. The single observation test is an efficient way to analyze how the observed information spreads to neighboring model grid points via the BE statistics. For the single observation test the perturbation potential temperature (T) was considered at a Latitude of 33.02^{o}N and Longitude of -116.93^{o}W and the first σ-level in domain-2 (d02), along with the pre-specified innovation (observation - background) value 1 K and with the error characteristic 1 K. The analysis increments (analysis – background) are analyzed in terms of spatial and vertical cross-sections within d02 as shown in Fig. 3. Here, three sets of experiments are conducted for the sensitivity study: (a) WRFDA-RBES1 (variance scale increased by 300% and length scale decreased by 75%), (b) WRFDA-RBES2 (variance scale increased by 100% and length scale decreased by 75%), and (c) WRFDA-RBES3 (variance scale increased by 25% and length scale decreased by 75%). Fig. 3 depicts that the analysis increments in WRFDA-RBES1 are higher up to 0.8 K in both spatial and vertical cross-sections. On the other hand, the analysis increments are 0.4 K and 0.6 K in WRFDA-RBES3 and WRFDA-

RBES2, respectively. Similar single observation tests were conducted for the horizontal wind components and moisture (Q_{vapor}), and consequently WRFDA-RBES1 produced higher analysis increments. A higher analysis increment implies that the analysis produced after data assimilation is closer to the observation. Based on the sensitivity test, WRFDA-RBES1 was chosen for the marine layer cloud simulation. For notational convenience, WRFDA-RBES1 is renamed to WRFDA from hereafter.

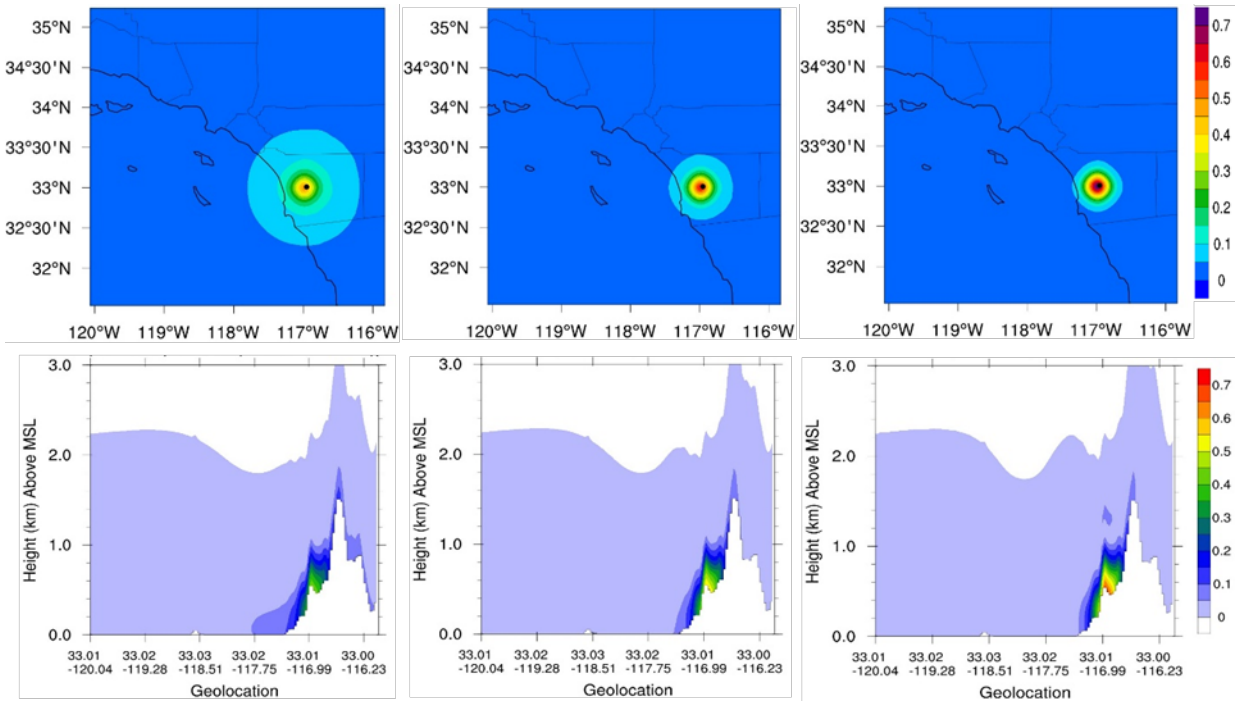

Figure 3: Analysis increments of perturbation potential temperature (T) at 1200 UTC, 12 June 2015 from the single observation (T) test by setting the innovation value 1 K and error 1 K at the observation location (black dot on top panel). Left panel: WRFDA-RBES3; center panel: WRFDA-RBES2; right panel WRFDA-RBES1. Top row: Bird's eye view of T at the first σ-level. Bottom row: Cross-section at latitude of 33°N.

3. Data Assimilation Experiments and Validation

3.1 Design of data assimilation experiments

We constructed three different sets of data assimilation experiments along with the WRF reference forecast (named as WRF). The three data assimilation experiments differ from each other based on the frequency of the assimilation time window. The details of the numerical

experiments are described in Table 1. The initial and boundary conditions are derived and downscaled from the NAM model, and the NAM data assimilation system is updated every six hours. With that in mind, the first data assimilation experiment assimilated all available conventional in-situ observations only once at the model initialization: i.e., 1200 UTC followed by a 6-h spin-up (named as WRFDA) and then forecasted for 24 h. The second data assimilation experiment assimilated all available conventional in-situ observations once at 0600UTC and again at 1200UTC (WRFDA-CYC-6hr) and then forecasted for 24 h. In the third data assimilation experiment the data assimilation was performed hourly starting at 0600UTC up to 1200UTC (WRFDA-CYC-1hr) and then forecasted for 24 h. The detailed configurations of the data assimilation experiments are described in Fig. 4.

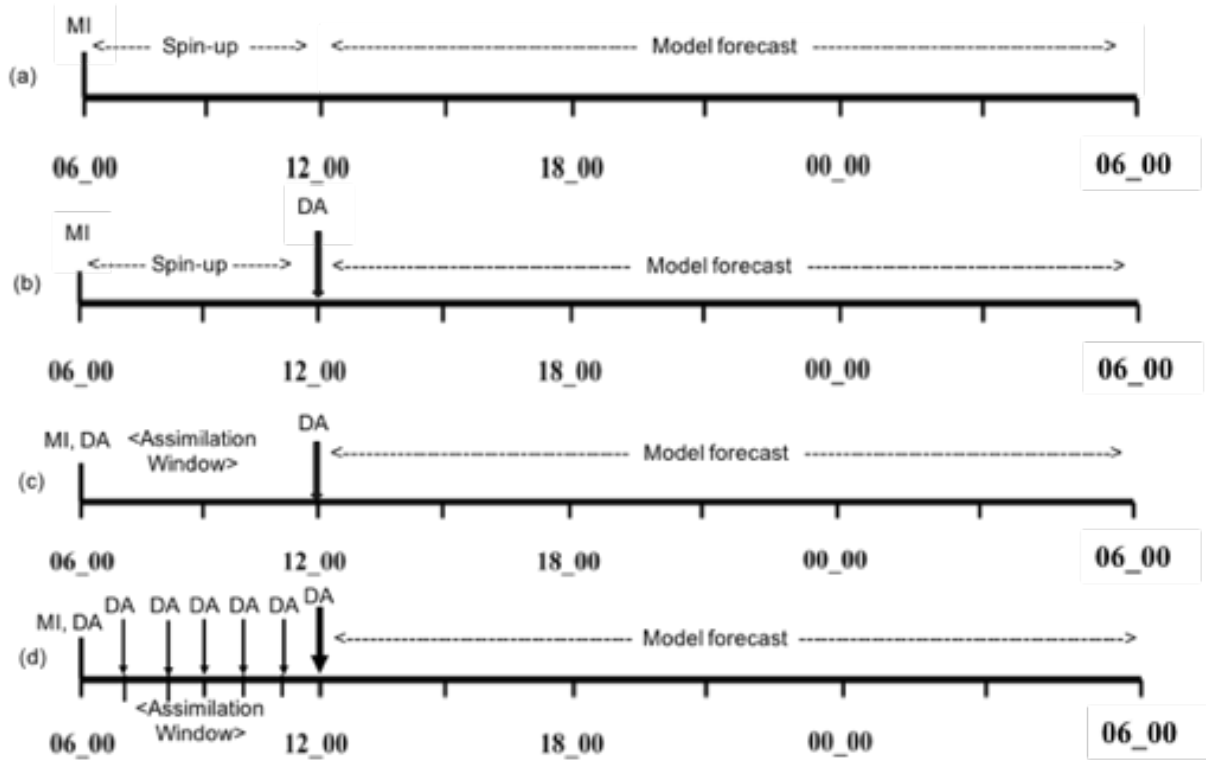

Figure 4: This diagram describes the design of WRF and data assimilation experiments and their data flow and assimilation windows for (a) WRF (b) WRFDA (c) WRFDA-CYC-6h and (d) WRFDA-CYC-1h. Here **MI** denotes model initialization and **DA** denotes data assimilation. The time (HH_MM) frames in the above diagram are in UTC.

Table 1: Detailed description of the numerical experiments.

Experiment Name	Descriptions
WRF	WRF simulation without data assimilation, initialized at 0600 UTC, with 0000 UTC NAM data (with 6-h spin-up from 0600 UTC to 1200 UTC) and run in forecast mode up to 0600 UTC, next day.
WRFDA	WRF run for 6-h spin-up from 0600 UTC to 1200 UTC and 3DVAR data assimilation applied at 1200 UTC, and run in forecast mode up to 0600 UTC, next day.
WRFDA-CYC-6hr	WRF initialized at 0600 UTC and 3DVAR data assimilation applied at every 6-h i.e., at 0600UTC and 1200 UTC during the spin-up period, with cyclic mode and run in forecast mode from 1200UTC to 0600 UTC, next day.
WRFDA-CYC-1hr	WRF initialized at 0600 UTC and 3DVAR data assimilation applied at every hour from 0600 to 1200 UTC during the spin-up period, with cyclic mode and run in forecast mode from 1200UTC to 0600 UTC, next day.

3.2 Synoptic descriptions of the marine layer days

In this study we have selected two sets of consecutive days with strong marine layer influence: (i) 02 and 03 June 2013 and (ii) 11 and 12 June 2015. For each day we analyzed the impact of 3DVAR data assimilation on model initialization and forecast of GHI and meteorological parameters associated with the variations in solar energy production. On 2nd June 2013, a trough of low pressure developed off the southern California coast, which strengthened onshore flow. The presence of a coastal eddy with a strong marine layer inversion makes the eddy more likely to push the marine layer clouds into inland valleys and clouds will remain near the coastline until the afternoon. According to the National Weather Service (NWS) report for San Diego at 0925 PDT 2nd June 2013, widespread low clouds were present over the coastal areas and San Diego valleys throughout the day (1200 PDT image is shown in Fig. 5a), which began to clear in the afternoon from east to west. The 1200 UTC, 02 June 2013 Miramar (NKX) sounding reported the marine layer was about 500 m deep with south winds below and south-west winds above a strong temperature inversion of 11 ^{o}C. The presence of a coastal eddy with a strong marine layer inversion promoted low clouds at the beaches throughout the day. On 03 June 2013, according to the 0900 PDT NWS report, marine layer low clouds covered the areas

west of the mountains inland to the coastal slopes of San Diego county and began to clear over the San Diego county valleys around 0900 PDT (Fig. 5b). The 1200 UTC, 03 June 2013 NKX sounding reported the marine layer was about 915 m deep with an 8 ºC temperature inversion (Fig. 6a). This represents an increase of about 415 m in the marine layer depth since the previous day. A weaker inversion supports clearing marine layer clouds, although some low clouds were expected to linger at the beaches into the afternoon.

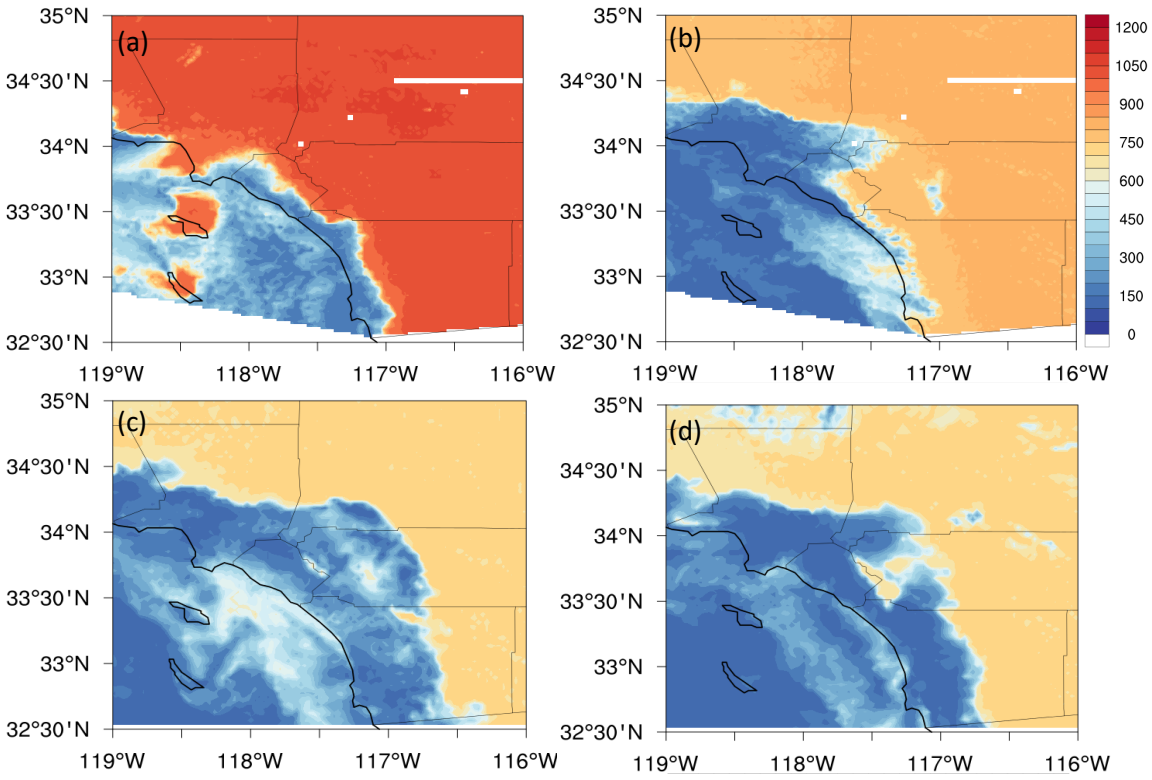

Figure 5: Spatial distribution of satellite derived (SolarAnywhere) GHI over southern California on (a) 1200 PDT, 02 June 2013, (b) 0900 PDT, 03 June 2013, (c) 0900 PDT, 11 June 2015, and (d) 0900 PDT, 12 June 2015.

On 11 June 2015, an upper level ridge of high pressure was building across the northern Mexican and southern Californian region. A moderate onshore flow was present over the region, which brought moderate diurnal marine layer intrusions inland and into valleys. The morning visible satellite imagery on 11 June 2015 showed widespread marine layer stratocumulus clouds covering the coast and far inland regions of the southern Californian coast (Fig. 5c). According to the 0845 PDT NWS report, a deep marine layer was observed with tops between 1200 m and 1370 m and bases as low as 250 m above mean sea level (MSL) over the region. The operational

NWP model suggested that the marine layer would be slow to break up and burn off and then consolidate along the coastline again in the afternoon. Similarly, according to the NWS, San Diego report at 0900 PDT, 12 June 2015, an upper level ridge was building across the region, creating significant warming inland and a shallower marine layer covering the coast and inland valleys (Fig. 5d). The 1200 UTC 12 June 2015, NKX Miramar sounding displayed a 7 ºC marine layer inversion (Fig. 6b), which supports low cloud persistence along the coast and inland valleys throughout most of the day. However, further inland areas cleared by late morning/early afternoon.

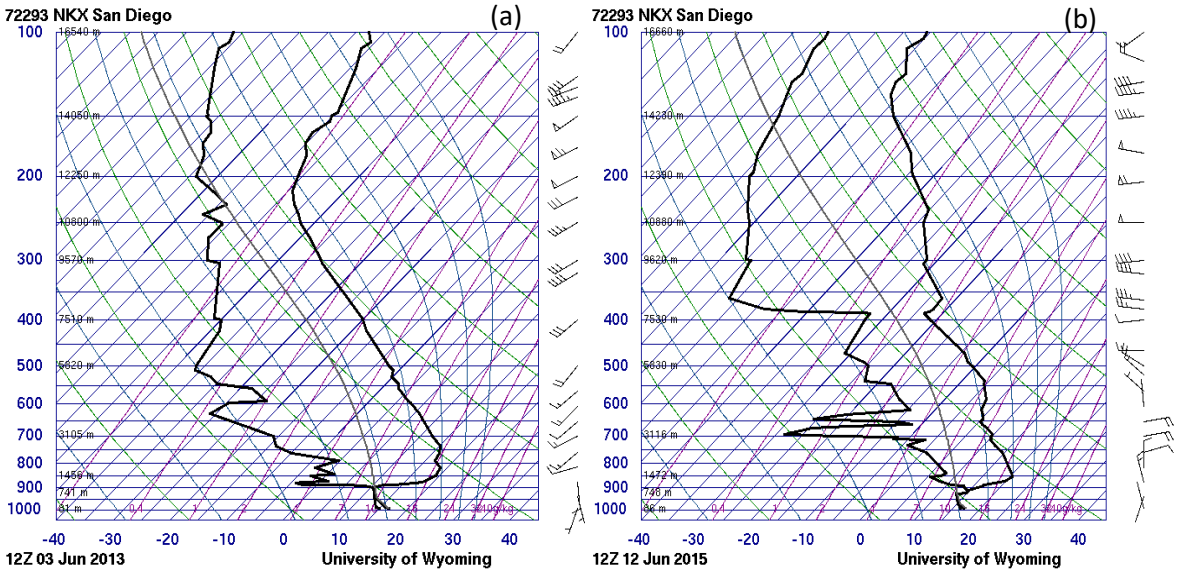

Figure 6: Skew-T diagram derived from MCAS, Miramar, San Diego (NKX) observations for (a) 1200 UTC 03 June 2013 and (b) 1200 UTC 12 June 2015. © University of Wyoming.

3.3 Observational data used for assimilation and validation

The meteorological observations used in the data assimilation experiments are obtained from National Oceanic and Atmospheric Administration's (NOAA) meteorological assimilation data ingest system (MADIS). The sources of observations assimilated in this study include surface observations, ships, and radiosonde networks. The observations assimilated in the data assimilation experiments are shown in Fig. 2 for a particular day. The assimilated meteorological parameters are temperature, dew point temperature, pressure, wind speed and direction from the above mentioned networks.

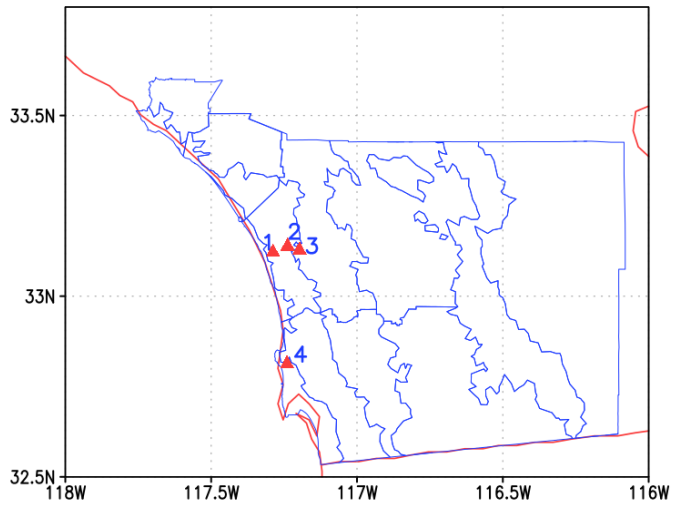

Figure 7: Map of San Diego County climate zones and four SDGE ground stations 1 (PWS1), 2 (PWS4), 3 (PWS6) & 4 (MSD) as described in Table 2.

Global horizontal irradiance (GHI) from four ground stations maintained by San Diego Gas & Electricity Company (SDGE) were used for model validation. The weather stations are located at varying distances from the coastline (Fig. 7, Table 2) to capture the gradient in cloud cover. Stations 1, 2 and 3 recorded averaged GHI measurements at 5-min resolution, while Station 4 recorded at 10-min resolution. Measurements from all stations were aligned with instantaneous WRF model outputs for validation and error estimation through linear interpolation. Additionally, Clean Power Research's SolarAnywhere (SolarAnywhere®, 2013) satellite data at 0.02 degree spatial resolution was used to analyze the spatial errors in the model simulated GHI parameter. The spatial analyses can extract more information about the spatial distribution of GHI biases.

The model forecasted errors for GHI are estimated and analyzed in terms of mean absolute error (MAE), mean bias error (MBE) and skill score (SS; Wilks 2006), defined as,

$$\text{MAE} = \frac{1}{N}\sum_{i=1}^{N}\left|x_i^{mod} - x_i^{obs}\right|, \quad (3)$$

$$\text{MBE} = \frac{1}{N}\sum_{i=1}^{N} x_i^{mod} - x_i^{obs}, \quad (4)$$

$$\text{and, SS} = 1 - \frac{MAE_{mod}}{MAE_{ref}}, \quad (5)$$

where, x_i^{mod} *and* x_i^{obs} are respectively the i^{th} model forecast and observed variables for a total sample of N number of data points in both temporal and spatial evaluations. Similarly, MAE_{mod} and MAE_{ref} are the MAE for the intra-day forecast from a particular model and reference forecast, respectively. The forecast skill score (FSS) is a measure of the percentage of forecast improvement/deterioration of a particular model simulation with respect to the reference forecast. The reference forecasts are alternatively the 24-h persistence forecast and the standard WRF simulation. The positive (negative) values of FSS indicate an improvement (deterioration) in the forecast for the corresponding variable with respect to the reference forecast.

Error terms were also computed for clear sky index (CSI). The CSI was computed by normalizing the GHI values with respect to the clear sky GHI values at the same time and location defined as below,

$$\text{CSI} = \frac{GHI}{GHI_{clearsky}}, \quad (6)$$

where $GHI_{clearsky}$ was obtained from the Kasten clear sky model (Ineichen and Perez, 2002; Perez et al., 2002). Errors based on the CSI give similar weights to all times of day, while GHI errors are more heavily weighted towards solar noon. Since marine layer stratocumulus are most prevalent in the morning, CSI errors are expected to more accurately differentiate forecast models that excel in marine layer stratocumulus forecasts.

Table 2: Detailed description of SDGE ground stations used for model validations.

Station name	**PWS1**	**PWS4**	**PWS6**	**MSD**
Latitude/ Longitude	33.12°N/ -117.29°W	33.14°N / -117.24°W	33.13°N / -117.20°W	32.81°N / -117.24°W
Elevation (m) from MSL	85	143	165	104
Distance from coastline (km)	3.8	9.3	12.2	2.7

4. Results and Discussions

4.1. Validation of initial profiles with sounding observations

In cloudy conditions NAM GHI is biased by up to 150 W m^{-2} (Mathiesen and Kleissl, 2011). NAM also underestimates the inversion base height and the liquid water content at model initialization, which reduces marine layer cloud formation under an otherwise suitable synoptic situation. Hence, for improved solar forecasting within a NWP model, better model initial profiles of the prognostic variables are needed. The model state variables are validated against Miramar (NKX: Lat 32.85°N/ Lon -117.12°W) radiosonde observations at the model initialization. The comparison of selected variables, such as equivalent potential temperature and relative humidity profiles, are shown in Fig. 8 for 12 June 2015. Figure 8 shows that the data assimilation experiments are closer towards the observation profile as compared to the WRF. WRFDA-CYC-1hr outperformed not only in simulating the initial profiles of equivalent potential temperature and relative humidity, but also temperature, mixing ratio, potential temperature, and other variables (not shown here). However, WRFDA-CYC-1hr data assimilation still exhibits biases in capturing the exact inversion base height as compared to the observations. The equivalent potential temperature and relative humidity profiles (Fig. 8), illustrate that the data assimilation experiments produced a secondary inversion layer, which might cause decoupling within the cloud layer and is conducive to thinner cloud layers as compared to the observations. This is evident in the relative humidity profiles (Fig. 8) which are saturated only up to 500 m versus over 700 m in the observations.

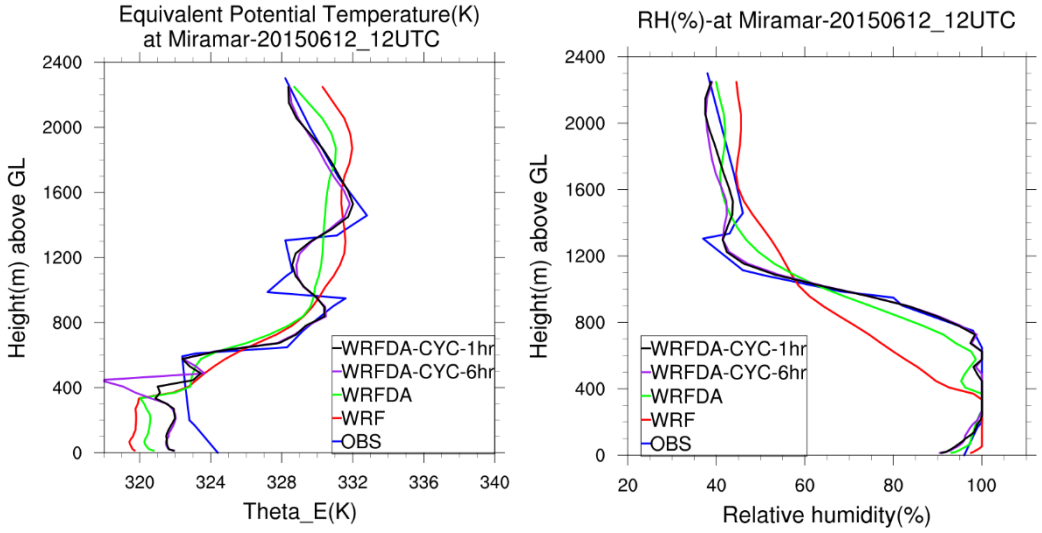

Figure 8: Validation of model simulated equivalent potential temperature (Theta_E) and relative humidity at model initialization at 12UTC, 12 June 2015 along with the radiosonde observations at MCAS, Miramar, San Diego. In the ordinate GL stands for "Ground Level".

4.2 Model validation for forecasted meteorological parameters and GHI

At first the surface (10 m) wind field and surface fluxes were considered in the model validation. Through advection of cool air from the ocean, the wind field contributes towards the development and advancement of marine layer clouds inland. Figure 9 depicts that WRFDA-CYC-1hr produced stronger onshore flows (westerly) across the southern California coast (especially the San Diego coast) during the early morning (at 1400 UTC) which helps to transport the marine layer stratocumulus clouds inland. On the other hand, WRF does not capture similar onshore flows during the early morning hours and the winds are rather weaker as compared to WRFDA-CYC-1hr. Other data assimilation experiments WRFDA and WRFDA-CYC-6hr are able to capture the onshore winds across San Diego coast during early morning hours. Although, the wind speeds are slightly weaker as compared to WRFDA-CYC-1hr (Fig. 9).

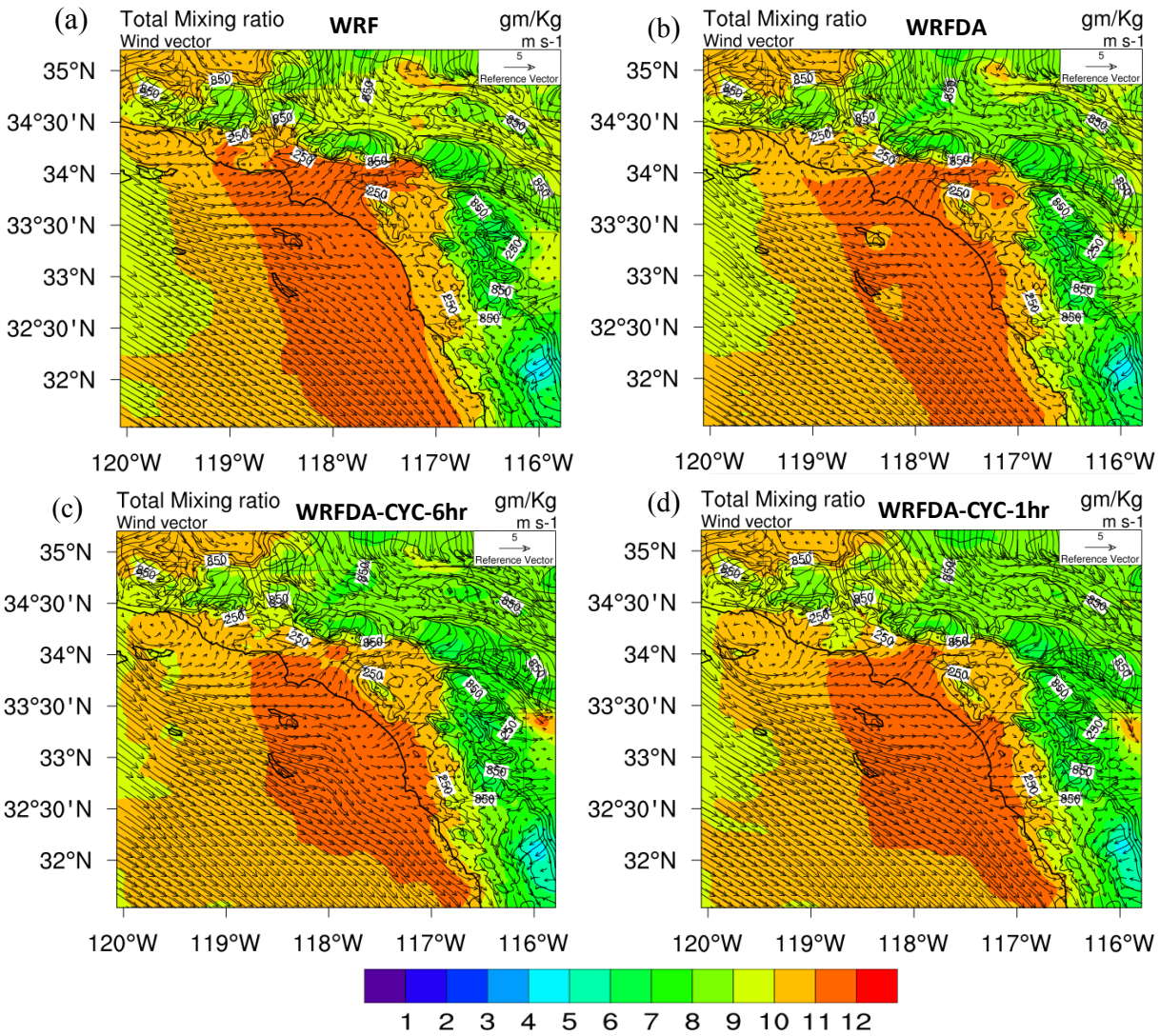

Figure 9: Spatial distributions of total mixing ratio (gm kg^{-1}; color) overlaid with terrain height contours (from 250 m to 1450m with 300m increment) and wind vectors (m s^{-1}) over domain-2 at 1400 UTC (0600 LST) from four different experiments on 12 June 2015 (a) WRF (b) WRFDA (c) WRFDA-CYC-6hr and (d) WRFDA-CYC-1hr.

Surface fluxes such as sensible heat flux (SHF) and latent heat flux (LHF) influence the marine layer clouds' life cycle over the coastal region by modulating heat and moisture input into the PBL. The model-simulated SHF and LHF in the coastal region from cyclic data assimilation experiments further support a thicker and more persistent marine layer cloud as compared to WRF. Due to the lack of observations near the southern Californian coast, it was not feasible to validate the model-simulated LHF and SHF.

The model-simulated GHI and liquid water content are analyzed at the four selected ground stations and a radiosonde location at MCAS, Miramar. GHI variations at coastal southern Californian regions during early summer are mostly affected by stratocumulus cloud cover, which reflects incoming solar radiation [Stephens and Greenwald, 1991; Chen et al., 2000]. The marine layer cloud optical thickness is directly proportional to the amount of LWC within the cloud layer. Thicker clouds during the early morning hours generally take longer to dissipate and thus reduce the average GHI. The time-height analysis of LWC from 12 June 2015 at MCAS, Miramar shows that WRFDA-CYC-6hr and WRFDA-CYC-1hr produced higher LWC and thicker cloud layers as compared to WRF and WRFDA simulations (Fig. 10). The clouds in WRF started to dissipate early at 1800 UTC and again formed around 2300 UTC, 12 June 2015 as shown in Fig. 10. The data assimilation experiments, especially WRFDA-CYC-1hr, produced a much thicker and more persistent cloud layer (Fig. 10d), in agreement with the MCAS, Miramar radiosonde profile at 0000 UTC, 13 June 2015 (Fig. 11). From the temperature, dewpoint temperature, and relative humidity profiles (Fig. 11) at 0000 UTC, 13 June 2015 from the MCAS, Miramar radiosonde, the marine layer cloud thickness was estimated to be about 300 m (from 300 m to 600 m above ground level), which is closer to the WRFDA-CYC-1hr experiment (Fig. 10d) when compared to others.

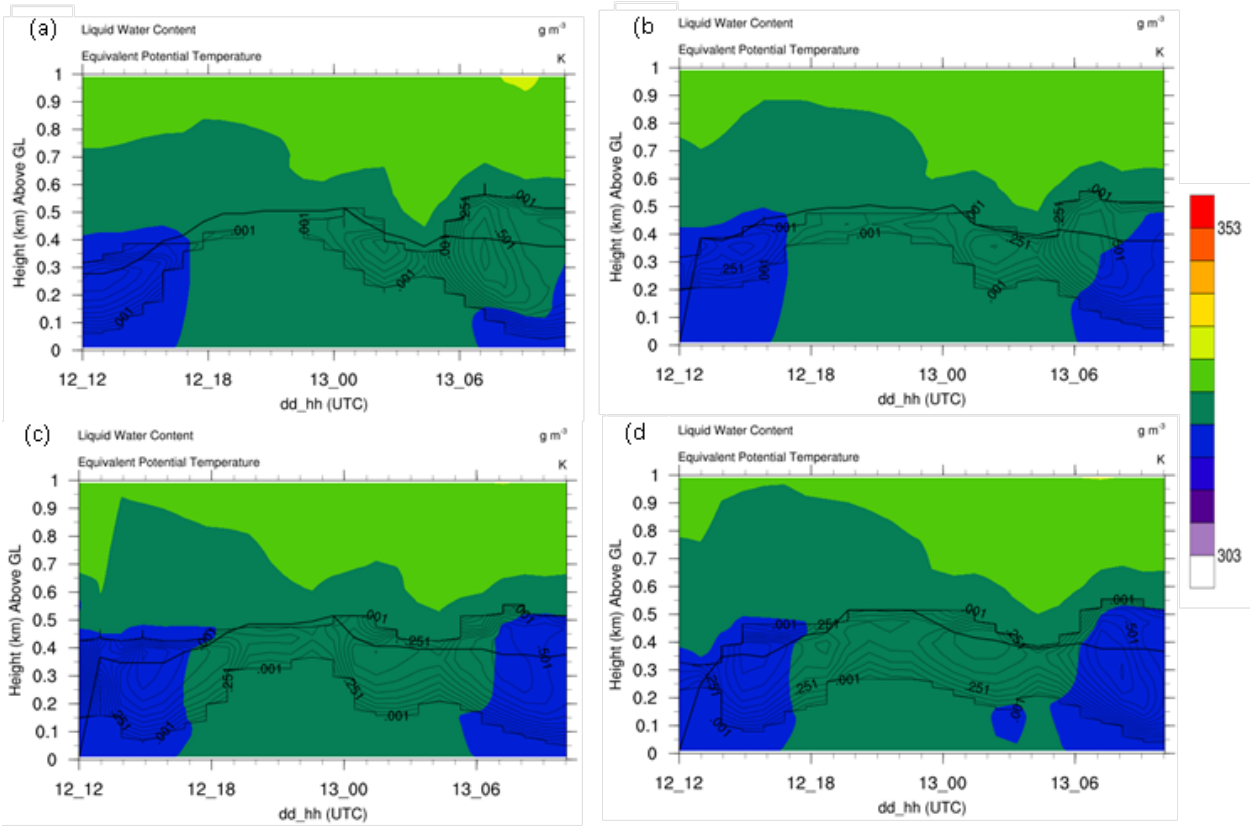

Figure 10: Time-height plot of liquid water content (LWC) at MCAS, Miramar (Lat 32.85N/ Lon -117.12W) from four different model simulations on 12 June 2015. The black line contours show the LWC from (a) WRF, (b) WRFDA, (c) WRFDA-CYC-6hr, and (d) WRFDA-CYC-1hr. The equivalent potential temperatures are shown in color.

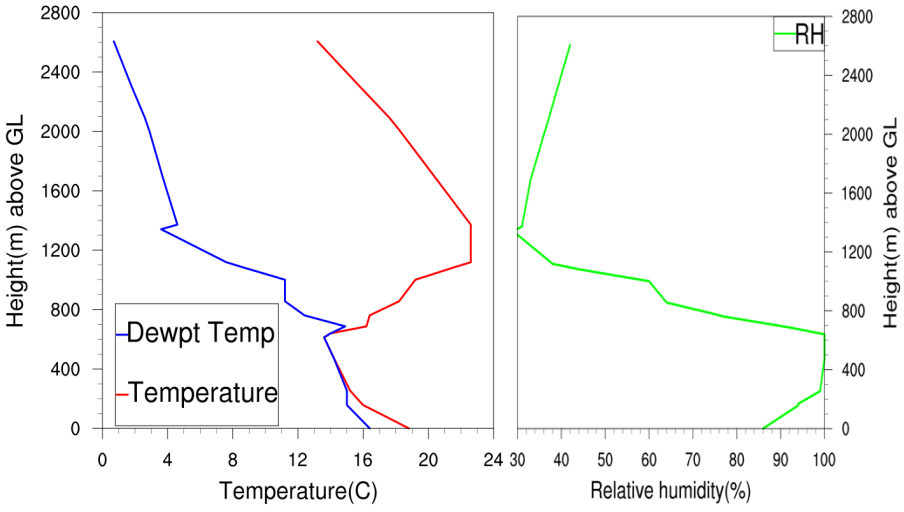

Figure 11: Vertical profiles of temperature (red line), dewpoint temperature (blue line) and relative humidity (green line) at 00UTC, 13 June 2015 from MCAS, Miramar radiosonde. In the ordinate GL stands for "Ground Level".

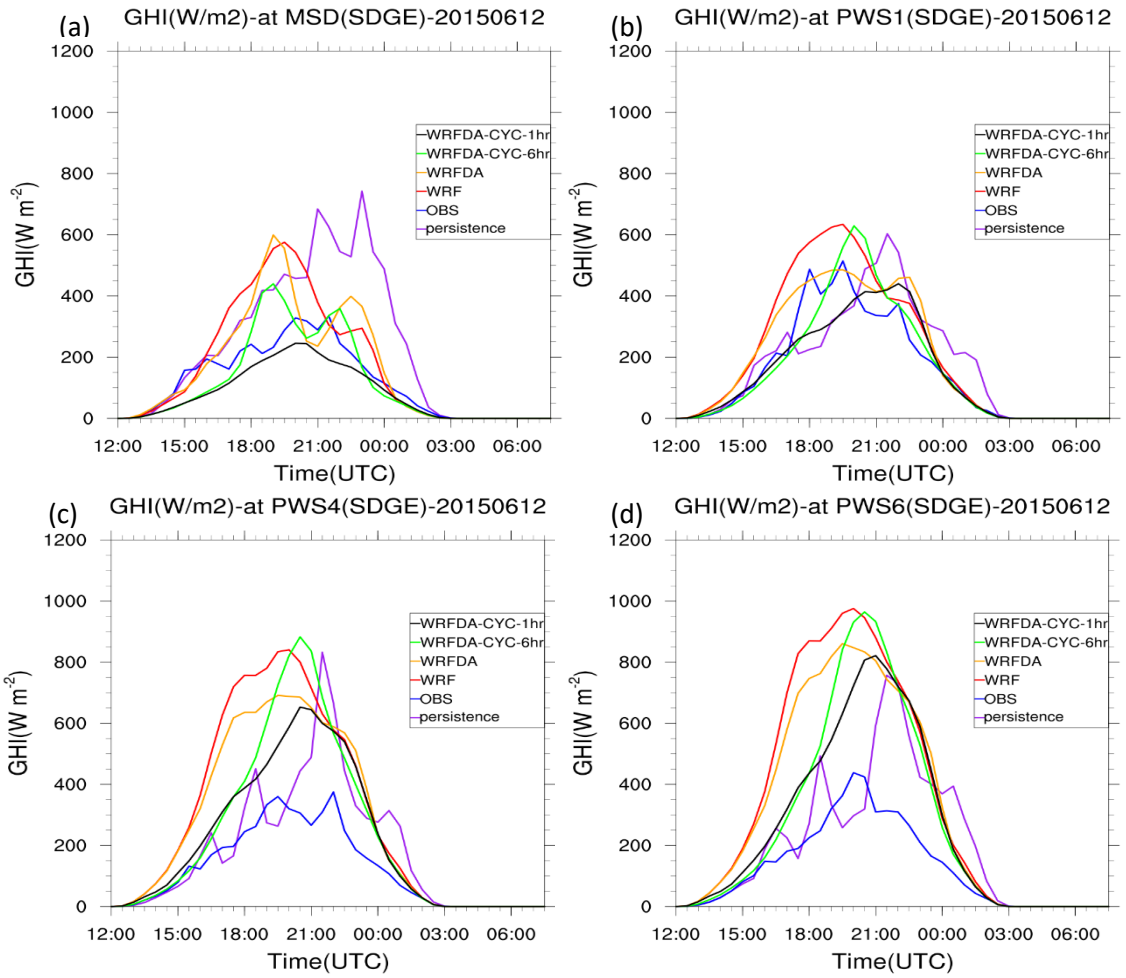

Figure 12: Validation of model-simulated GHI (W m^{-2}) time series for an intra-day forecast from all four experiments along with the measurements from four SDGE ground stations (a) MSD (b) PWS1 (c) PWS4 and (d) PWS6 on 12 June 2015.

4.3 Model validation with ground station observations

The forecasted GHI from WRF and data assimilation experiments are validated against the observed GHI at four SDGE ground stations (locations mapped in Fig. 7) on 12 June 2015 as shown in Fig. 12. The cyclic data assimilation experiments consistently simulated GHI values closer to the observations when compared to WRF and WRFDA. The MAE in GHI forecasts from the cyclic data assimilation experiments are significantly lower when compared to WRF and WRFDA at all four validated ground stations as shown in Fig. 13. At the two coastal stations (MSD and PWS1), the model simulations for GHI outperformed the 24-h persistence forecast by reducing the MAE values by 50-100 W m^{-2}. Here, the 24-h persistence forecasts are simply the

observed GHI values from the same time on the previous day. The selection of case study days was partially motivated by the fact that they were consecutive marine layer days. The averaged MAE and FSS of all four stations in intra-day GHI forecast (Fig. 13c) confirm that the MAE values from cyclic data assimilation outperformed WRF and WRFDA. WRFDA-CYC-1hr came out as the top performer with the mean FSS of 20% with reference to 24-h persistence forecast. On the other hand, WRF and WRFDA deteriorate the forecast by a range of up to -40% (Fig. 13c).

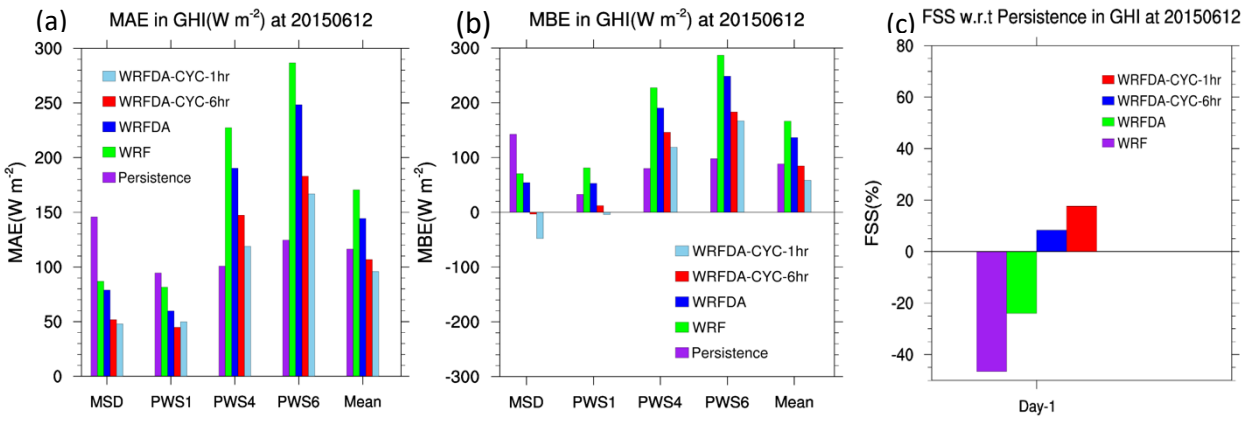

Figure 13: (a) MAE and (b) MBE in GHI intra-day forecast are estimated at MSD, PWS1, PWS4, PWS6, and mean of all four stations (Mean) on 12 June 2015 (c) FSS verses 24-hr persistence in GHI averaged over all four ground stations on 12 June 2015.

The cyclic data assimilation experiments also produced the early morning cloudy conditions consistently better than the WRF and WRFDA, as observed in CSI time series (Fig 14). The MAE, MBE, and FSS in CSI intra-day forecast are estimated at four ground stations and averaged over all four stations on 12 June 2015 (Fig. 15). The MAE values in CSI intra-day forecasts from cyclic data assimilation are significantly reduced, especially from the WRFDA-CYC-1hr experiment. The hourly assimilation of meteorological observations brings the model initial profiles closer to the observations, which helps to represent the state of the atmosphere more accurately and produce thicker marine layer clouds as compared to the other experiments. The ranking of the models from GHI forecasts also holds for CSI forecasts (Fig. 14 & 15). WRFDA-CYC-1hr produced the lowest CSI MAE value at below 0.2, which corresponds to an

improvement of 18% w.r.t. 24-h persistence forecast in CSI. On the other hand, WRF and WRFDA shows deterioration of the forecasts by -30% (Fig. 15c).

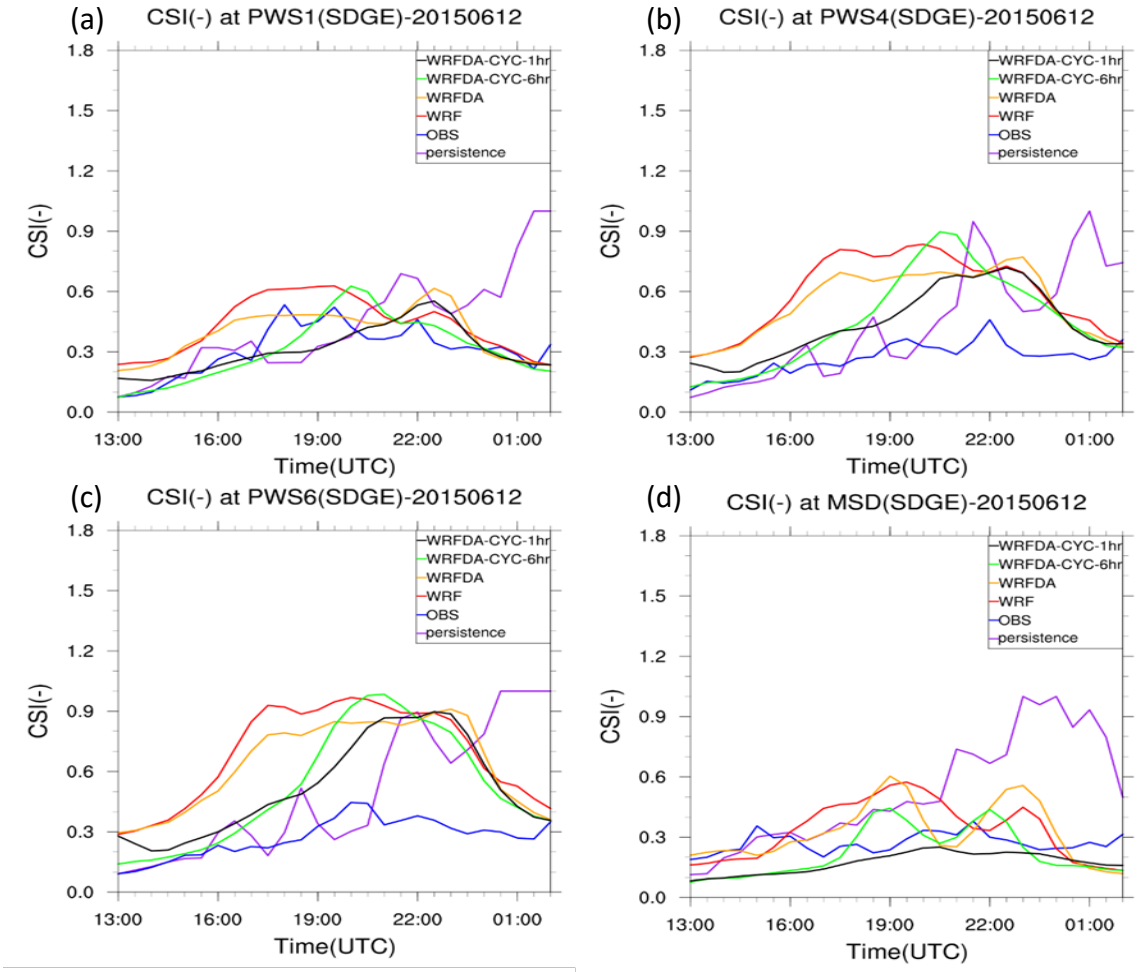

Figure 14: Validation of CSI time series for intra-day forecast at four ground stations: PWS1, PWS4, PWS6 and MSD for 12 June 2015.

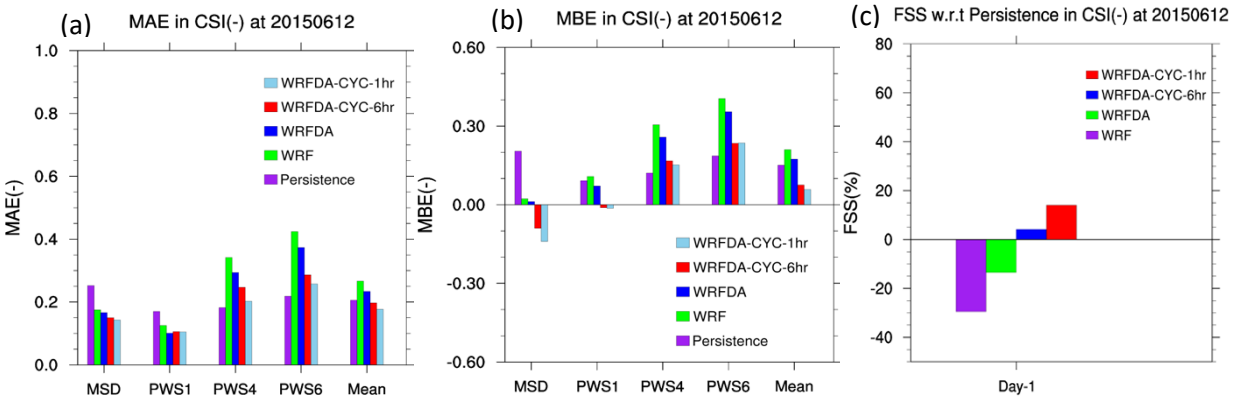

Figure 15: (a) MAE and (b) MBE in CSI for intra-day forecasts are estimated at MSD, PWS1, PWS4, PWS6 and mean of all four stations (Mean) on 12 June 2015 (c) FSS verses 24-hr persistence in CSI averaged over all four ground stations on 12 June 2015.

Table-3: MAE averaged over four case study days (02 June 2013, 03 June 2013, 11 June 2015 and 12 June 2015) for intra-day GHI and CSI forecasts at all four stations.

	MAE in GHI forecast [W m-2]					MAE in CSI forecast [-]				
	Persistence	**WRF**	**WRFDA**	**WRFDA-CYC-6hr**	**WRFDA-CYC-1hr**	**Persistence**	**WRF**	**WRFDA**	**WRFDA-CYC-6hr**	**WRFDA-CYC-1hr**
MSD	170	153	154	103	112	0.27	0.24	0.26	0.19	0.21
PWS1	159	179	164	105	83	0.27	0.29	0.28	0.19	0.15
PWS4	171	229	216	161	136	0.29	0.39	0.37	0.28	0.22
PWS6	174	191	178	134	117	0.31	0.34	0.32	0.25	0.19

Table-4: MBE averaged over four case study days (02 June 2013, 03 June 2013, 11 June 2015 and 12 June 2015) for intra-day GHI and CSI forecasts at all four stations.

	MBE in GHI forecast					MBE in CSI forecast				
	Persistence	**WRF**	**WRFDA**	**WRFDA-CYC-6hr**	**WRFDA-CYC-1hr**	**Persistence**	**WRF**	**WRFDA**	**WRFDA-CYC-6hr**	**WRFDA-CYC-1hr**
MSD	21	57	51	-20	-46	0.03	0.03	0.03	-0.08	-0.15
PWS1	32	163	144	43	4	0.07	0.24	0.22	0.06	0.03
PWS4	57	214	206	146	98	0.11	0.35	0.33	0.23	0.16
PWS6	47	173	163	109	72	0.11	0.28	0.27	0.18	0.12

The mean MAE and FSS of all four case study days (02 June 2013, 03 June 2013, 11 June 2015 and 12 June 2015) are estimated at all four stations separately and given in Table 3. The results indicate that MAE values in GHI and CSI from cyclic data assimilation experiments are significantly reduced compared to WRF, WRFDA, and 24-h persistence forecasts at all four analyzed stations. The maximum reduction in MAE values in both GHI and CSI forecasts are obtained at the coastal stations (MSD and PWS1). The lowest MAE values in intra-day GHI and CSI forecast are 83 W m^{-2} and 0.15, respectively, at PWS1 from WRFDA-CYC-1hr (Table 3).

Similarly, the lowest MBE in GHI and CSI forecasts are obtained from WRFDA-CYC-1hr of 4 W m^{-2} and 0.03, respectively, at PWS1 (Table 4). The original WRF simulation is more positively biased at all four stations compared to other simulations followed by WRFDA. This bias reflects the inability of WRF to generate a thick stratocumulus cloud layer due to inaccurate initial moisture profiles. This stratocumulus case is better specified in the cyclic data assimilation experiment because of the more accurate initial moisture profile, that is updated in a regular interval using in-situ observations. The 24-h persistence forecast is the least biased in intra-day GHI and CSI forecast at all three stations except PWS1 (Table 4). The average FSS of all four case study days' w.r.t 24-h persistence and WRF are estimated at each station and given in Table 5 & 6, respectively. The maximum FSS in GHI and CSI forecast w.r.t. 24-h persistence is 39.4% and 40.7% respectively at PWS1 from WRFDA-CYC-1hr followed by WRFDA-CYC-6hr. Similarly, the maximum FSS in GHI and CSI forecast w.r.t. WRF is 50.4% at PWS1 and 45.6% at PWS4 from WRFDA-CYC-1hr (Table 6). The hourly cyclic assimilation has particularly positive values of FSS (superior forecast) w.r.t 24-h persistence at all four stations, and the coastal stations (MSD and PWS1) have higher FSS compared to the inland stations (Table 5). The lower FSS at inland stations is due to the lack of transport of the marine layer stratocumulus clouds far inland, which is a typical shortcoming of marine layer cloud forecasting over the southern Californian coast. Many factors might be responsible, including the correct representation of the advection terms and coefficients within the model dynamics, the accurate estimation of inversion base height from the PBL parameterization, and the accurate parameterization of the cloud top entrainment and radiative cooling. However, WRF and WRFDA have mostly negative values of FSS (inferior forecast) w.r.t. 24-h persistence at all four stations. All three data assimilation experiments have positive values of FSS (superior forecast) w.r.t WRF in GHI and CSI forecast at all four stations, except WRFDA at MSD station.

The minimum MAE in GHI and CSI forecasts away from the coast is 117 W m^{-2} and 0.19 respectively at PWS6 (Table 3) from WRFDA-CYC-1hr. However, the minimum MBE in GHI and CSI forecasts away from the coast is estimated at 47.5 W m^{-2} and 0.11, respectively, from the 24-h persistence forecast. All four WRF simulations are positively biased in GHI and CSI forecasts at all four analyzed stations, except the cyclic data assimilation experiments at MSD, the station closest to the coast line. In other words, the cyclic data assimilation produced thicker stratocumulus cloud layers near the beaches, but higher topography seems to limit the cloud

thickness further inland. Deeper inland coverage of the thicker stratocumulus cloud layer from the cyclic assimilation is also caused by stronger onshore wind circulation along the coastline. The maximum FSS in GHI and CSI forecasts at inland stations w.r.t. 24-h persistence are 13.0% and 26.9%, respectively, at PWS6 from WRFDA-CYC-1hr experiment (Table 5). Similarly, the maximum FSS in GHI and CSI forecasts at inland stations w.r.t. WRF is 41.24% and 45.6%, respectively, at PWS4 from WRFDA-CYC-1hr experiment (Table 6).

Table-5: FSS w.r.t. 24-h persistence forecast averaged over all four case study days (02 June 2013, 03 June 2013, 11 June 2015 and 12 June 2015) for intra-day GHI and CSI forecast at all four stations.

	FSS w.r.t. Persistence in GHI forecast				FSS w.r.t. Persistence in CSI forecast			
	WRF	WRFDA	WRFDA-CYC-6hr	WRFDA-CYC-1hr	WRF	WRFDA	WRFDA-CYC-6hr	WRFDA-CYC-1hr
MSD	-6.06	-6.26	26.9	29.68	11.93	4.34	27.86	18.62
PWS1	-28.4	-17.2	19.87	39.4	-7.74	-3.24	25.52	40.69
PWS4	-65.69	-54.68	-17.04	3.6	-50.44	-39.9	-10.47	17.11
PWS6	-42.82	-33.94	-0.31	13.03	-26.87	-19.9	5.74	26.93

Table-6: FSS w.r.t. WRF averaged over all four case study days (02 June 2013, 03 June 2013, 11 June 2015 and 12 June 2015) for intra-day GHI and CSI forecast at all four stations.

	FSS w.r.t. WRF in GHI forecast			FSS w.r.t. WRF in CSI forecast		
	WRFDA	WRFDA-CYC-6hr	WRFDA-CYC-1hr	WRFDA	WRFDA-CYC-6hr	WRFDA-CYC-1hr
MSD	0.43	32.37	31.7	-7.97	19.6	9.16
PWS1	9.72	32.29	50.39	3.68	19.7	35.38
PWS4	4.72	28.43	41.24	5.51	27.18	45.6
PWS6	3.91	25.71	40.01	4.47	23.83	44.13

4.4. Stratocumulus cloud-base tendency

Utilizing the mixed-layer model framework originally developed by Lilly (1968), the time tendency of cloud base $\overline{\frac{\partial z_b}{\partial t}}$ can be expressed as a linear combination of the tendencies of heat and moisture (Ghonima et al., 2015):

$$\overline{\frac{\partial z_b}{\partial t}} = \frac{\partial z_b}{\partial \theta_l}\overline{\frac{\partial \theta_l}{\partial t}} + \frac{\partial z_b}{\partial q_t}\overline{\frac{\partial q_t}{\partial t}}, \quad (7)$$

where the response of cloud base to heat $\frac{\partial z_b}{\partial \theta_l}$ and moisture $\frac{\partial z_b}{\partial q_t}$ is described in Ghonima et al. (2015), and the tendencies of liquid water potential temperature $\overline{\frac{\partial \theta_l}{\partial t}}$ and total water mixing ratio $\overline{\frac{\partial q_t}{\partial t}}$ are obtained from the budget equations derived in Appendix A of Ghonima et al. (2016). In summary, the tendency of heat at a fixed location is a linear combination of heat advected by the mean wind (computed with centered finite differencing), sensible heat flux provided by the surface (obtained from the land surface model), radiative forcing (obtained from the radiative parameterization), and entrainment warming. The entrainment warming term is obtained as the residual when comparing the actual heat tendency in WRF with the heat tendency computed with just the advection, surface heating, and radiative forcing terms. Similarly, the tendency of moisture at a fixed location is a linear combination of moisture advected by the mean wind, latent heat flux from the surface (from the land surface model), and entrainment drying (again taken as the residual). Rain does not occur in the considered simulations, so it is neglected in the moisture tendency.

Figure 16 shows cloud base $\overline{z_b}$ tendencies for 12 July, 2015 from 0600 to 0000 PST for all configurations at the coastal ground station PWS1, with a breakdown of the $\overline{z_b}$ tendencies derived from the moisture (left) and heat (center) budgets, alongside the total $\overline{z_b}$ tendency (right). Positive (negative) $\overline{z_b}$ tendency indicates cloud thinning (thickening). Figure 16 shows the heat budget dominating the $\overline{z_b}$ tendency. The primary difference between all configurations can be seen in the total $\overline{z_b}$ tendency at about 0600 PST (approximately sunrise): in WRF, the cloud deck is thinning, whereas in WRFDA, the cloud deck is not changing significantly, and in both WRFDA-CYC-6hr and WRFDA-CYC-1hr, the cloud deck is thickening. The main factor sustaining the cloud in this case is the advection of cool, moist air from the ocean, which is indicated by negative $\overline{z_b}$ tendencies produced by the advective terms (in green). This advection

593 contribution is demonstrated in Figure 9, where simulations utilizing data assimilation predict
594 stronger onshore wind in the San Diego coast region (approximately 33°N, 117°W), especially
595 WRFDA-CYC-1hr. On July 12, all WRFDA simulations predicted thicker cloud cover, which
596 reduces the surface heating (red) to the boundary layer through the suppression of down-welling
597 shortwave radiation at the surface. Average $\overline{z_b}$ tendencies over all four case study days are also
598 estimated and shown in Figure 17, the primary difference again being the advection of cool,
599 moist air evident in the WRFDA configurations. Over the study period, all WRFDA simulations
600 produced thicker clouds on average, leading to reduced surface heating (red) as well as increased
601 radiative cooling (dashed magenta) due to stronger longwave emission (and hence cooling) by
602 the thicker cloud decks. These effects are strongest in the WRFDA-CYC-1hr configuration,
603 causing it to predict thicker clouds with longer lifetimes.

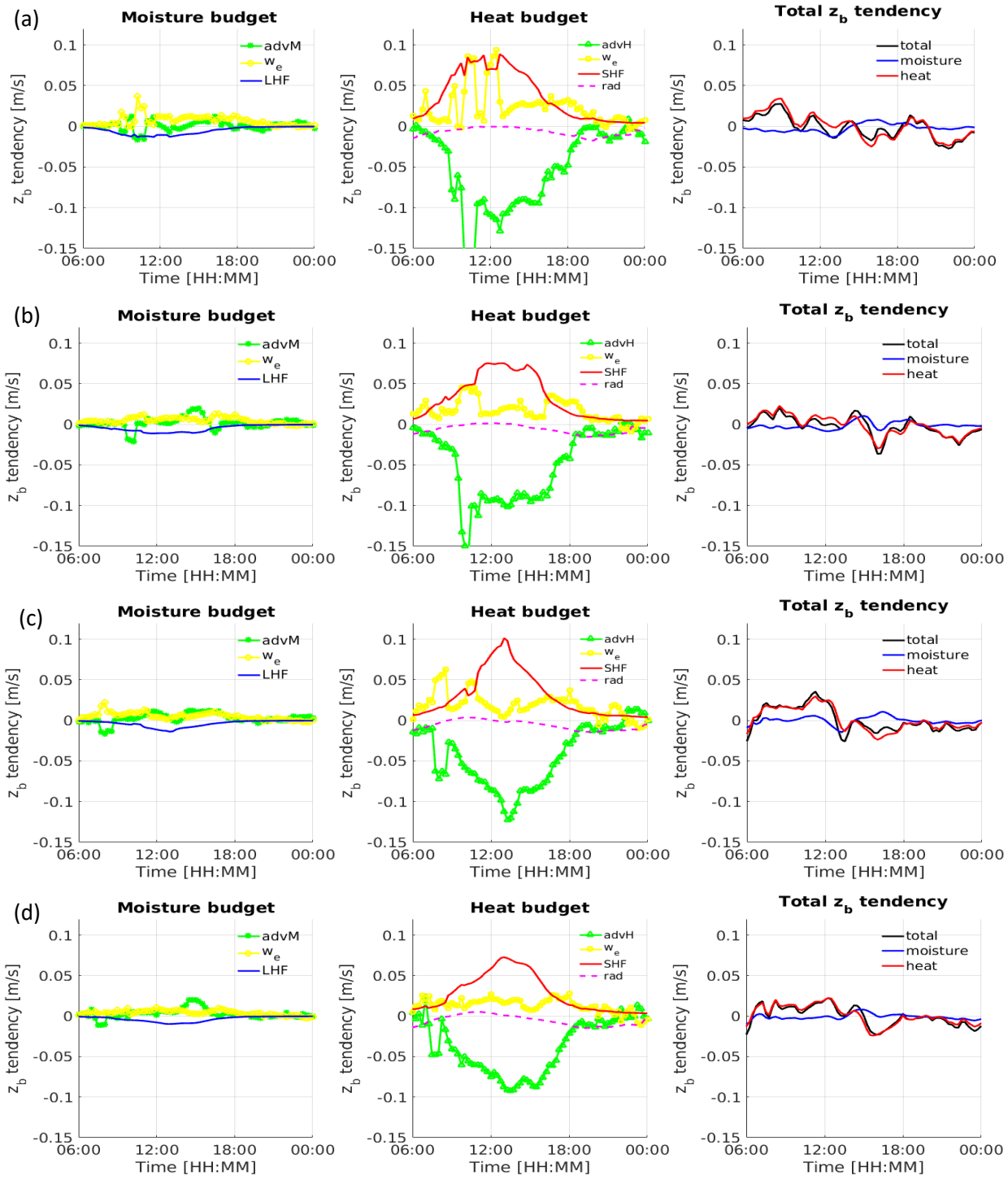

Figure 16: Cloud-base tendency with reference to the thermodynamic parameters at PWS1 from (a) WRF, (b) WRFDA, (c) WRFDA-CYC-6h and (d) WRFDA-CYC-1hr experiments on 12 June 2015.

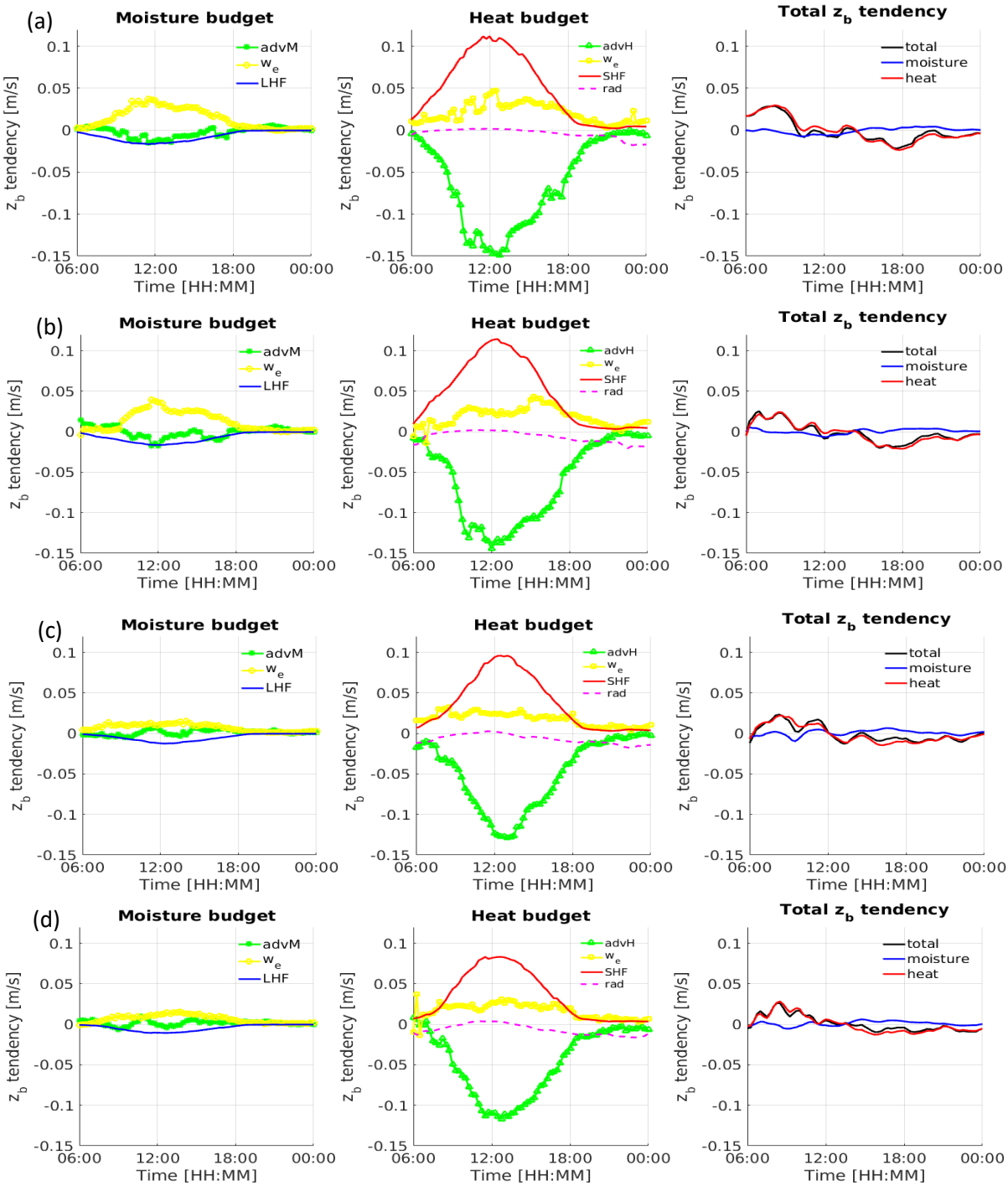

Figure 17: Mean Cloud-base tendency of all four case study days with reference to the thermodynamic parameters at PWS1 from (a) WRF, (b) WRFDA, (c) WRFDA-CYC-6h and (d) WRFDA-CYC-1hr experiments.

614 ***4.5 Model validation with satellite observations***

615 The spatial distributions of daily mean MAE and MBE in GHI forecasts averaged over all
616 four case study days are analyzed against the SolarAnywhere gridded satellite measurements and
617 shown in Figs. 18 & 19 respectively. Similar analyses are also conducted for CSI forecasts, but
618 not shown here. It is noted that the magnitude of MAE in GHI forecasts over the southern
619 Californian coast are significantly less in WRFDA-CYC-1hr compared to other simulations
620 including the 24-h persistence forecast. This difference is especially significant over San Diego
621 and Orange County as shown in Fig. 18. The MAE in GHI forecast from WRFDA-CYC-1hr is
622 reduced by 100 to 150 W m^{-2} as compared to 24-h persistence and other simulations. The higher
623 values of MAE in GHI forecast are noted near the coastline, as those areas are more prone to
624 marine layer stratocumulus clouds. A similar pattern of spatial distributions of MAE in CSI
625 intra-day forecast is also noted (not shown here). The WRFDA-CYC-1hr produced significantly
626 lower MAE values in both GHI and CSI intra-day forecast over the San Diego county coastal
627 areas compared to other simulations including 24-h persistence forecast. The higher values of
628 MAE in both GHI and CSI persistence forecasts resulted from significant variations in the day-
629 to-day stratocumulus cloud patterns over the southern Californian coast.

630 The spatial distributions of MBE in GHI forecasts describes the regions with positive and
631 negative biases in intra-day forecast as shown in Fig. 19. The persistence forecasts mostly have
632 small bias errors. All four model simulations show mostly positive biases (i.e., overestimation of
633 stratocumulus clouds) over the ocean and negative biases (i.e., underestimation of stratocumulus
634 clouds) over land. Similar patterns of biases are noted in the spatial distributions of MBE in CSI
635 intra-day forecasts (not shown here). Higher positive biases in both GHI and CSI intra-day
636 forecasts over the coastal land region are observed from WRF and WRFDA. Cyclic data
637 assimilation significantly reduces the positive biases over the coastal land region (Fig. 19).
638 Biases in GHI and CSI forecasts obtained from the hourly cyclic data assimilation experiment
639 reduced to zero near the coastline and inland areas of San Diego and Los Angeles county. Cyclic
640 data assimilation produced comparatively higher negative biases in both GHI and CSI intra-day
641 forecasts over the ocean and lesser positive biases over land near the coastline (Fig. 19),
642 indicating that cyclic data assimilation produced thicker marine layer stratocumulus clouds over

the ocean, and the stronger onshore wind flow helps to transport the cloud layers inland compared to the WRF and WRFDA simulations.

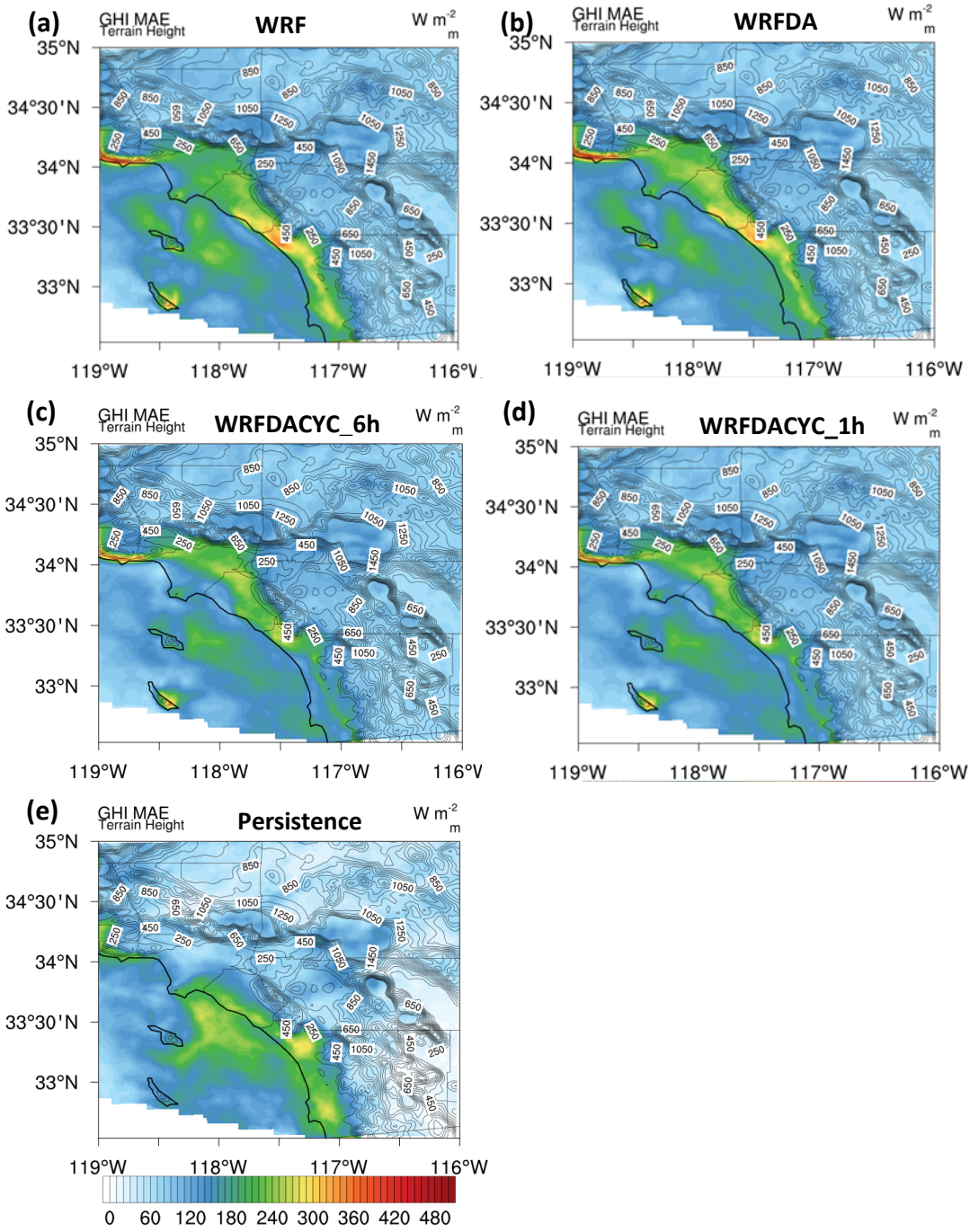

Figure 18: Spatial distributions of the daily mean MAE in GHI forecasts averaged over all four case study days, estimated from SolarAnywhere gridded satellite measurements.

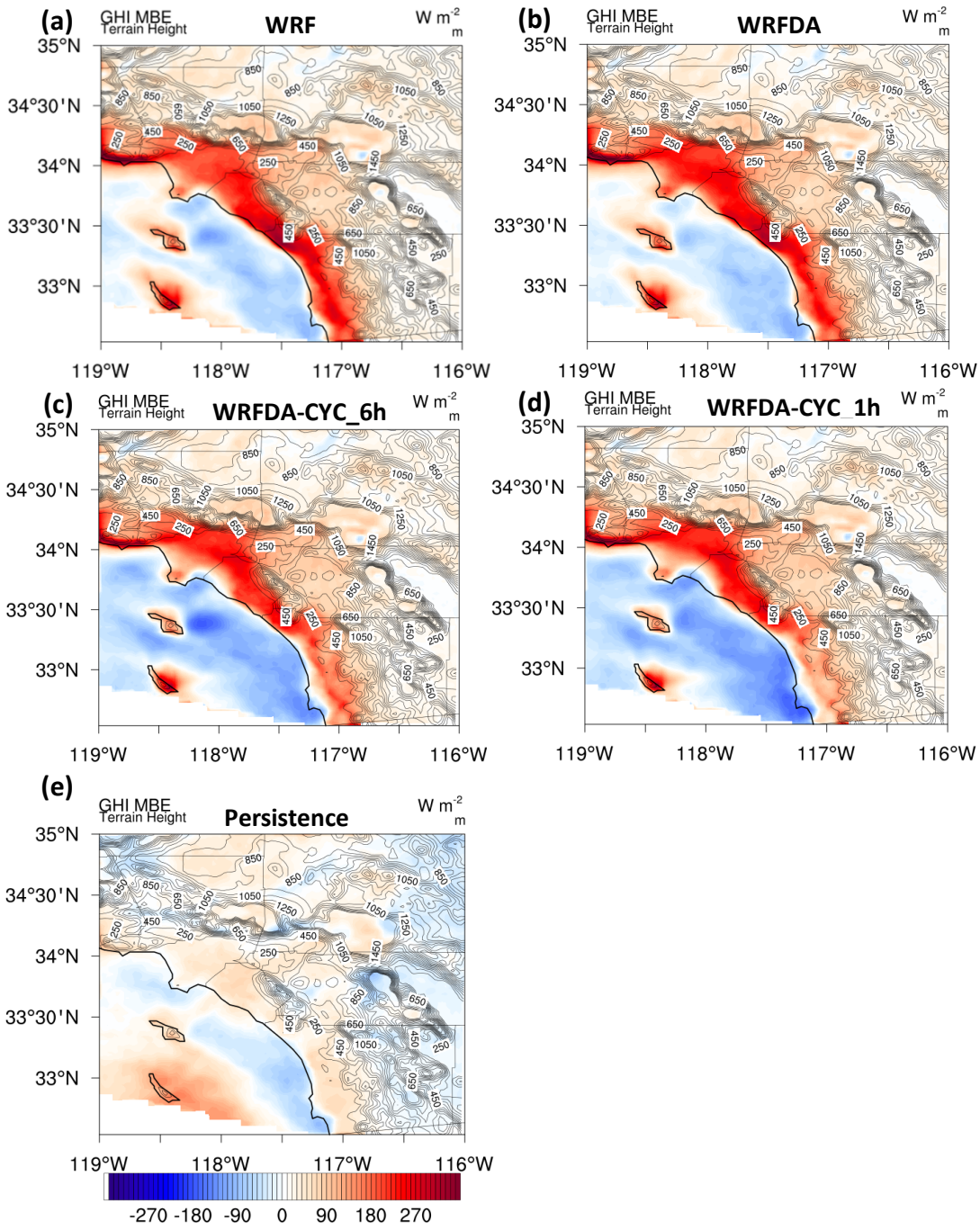

Figure 19: Spatial distributions of daily mean MBE in GHI forecasts averaged over all four case study days, estimated from SolarAnywhere gridded satellite measurements.

5. Conclusions

This study examined the impact of assimilating in-situ conventional observations (such as surface observations, ships, and radiosonde) on NWP model initialization and intra-day GHI and CSI forecasts with three different configurations of data assimilation experiments (Section 3). The results are benchmarked against 24-h persistence forecasts and standard WRF simulations. The near-surface observations are important sources of information about lower tropospheric weather phenomena and have been very crucial for weather forecasting. Here, we have used these observations as input to simulate marine layer stratocumulus cloud in an NWP model. Solar radiation and other meteorological parameters associated with the marine layer stratocumulus clouds over the southern California coast are examined. The GHI and CSI intra-day forecasts have been validated against SDGE ground measurements and SolarAnywhere satellite measurements. Hourly cyclic assimilation of in-situ observations outperformed the rest of the model simulations and a 24-h persistence forecast.

Earlier studies (Mathiesen & Kleissl 2013; Yang & Kleissl 2016; Zhong et al., 2017) found that the WRF model initialized with NAM reanalysis data showed significant biases in surface irradiance, temperature, and moisture forecasts. It can be inferred that the model initialization errors derived from NAM data propagated to the model forecasts and appeared in the forecast biases. In NWP models, the accuracy of forecasts significantly depends on the accuracy of the initial state of model variables. Hence, the 3DVAR data assimilation technique was employed within the WRF model to obtain an accurate initial state by customizing suitable tuning parameters of length scale and variance scale through a sensitivity test. From the initial validation, it was found that the model initial profiles of all the prognostic parameters from WRFDA-CYC-1hr are significantly closer to the radiosonde observations compared to the rest of the experiments. The hourly assimilation of in-situ observations also significantly improved both the spatial coverage and life time of marine layer stratocumulus clouds over the southern Californian coast.

The six hourly cyclic assimilation was the second best performer. It can be noted that, due to the absence of liquid water content at model initialization, clouds develop slowly from the evolution of microphysical processes during the model spin-up resulting in underestimation of stratocumulus cloud cover as compared to observations. The hourly data assimilation during the model spin-up updates and enhances the moisture field and subsequently the liquid water content

687 in regular intervals. Hence, WRFDA-CYC-1hr forecasted thicker stratocumulus cloud cover and
688 longer life time compared to WRFDA and WRF results. Near-surface wind circulations over the
689 southern Californian coast have been improved due to cyclic data assimilation (WRFDA-CYC-
690 1hr) compared to WRFDA and WRF, promoting transport of marine layer stratocumulus clouds
691 farther inland across the coastline. The MAE in GHI and CSI forecasts at the coastal stations
692 were significantly less than at the inland stations. The MAE and MBE analyses for GHI and CSI
693 forecasts indicated that the cyclic data assimilation experiments simulated thicker clouds at the
694 coastal stations compared to the inland stations. This result indicates that the data assimilation
695 experiments still fall short in simulating thicker stratocumulus cloud layers' transport farther
696 inland, causing premature dissipation. Thus, the thinner inland clouds dissipated faster after
697 sunrise due to high surface heat fluxes and cloud top entrainment. It has been noted that, at the
698 farther inland stations, the hourly cyclic data assimilation experiment produced thicker marine
699 layer clouds as compared to WRF. The spatial distributions of model biases have been estimated
700 against SolarAnywhere satellite measurements, showing overprediction of stratocumulus cloud
701 cover over the ocean and underprediction over land. Marine layer stratocumulus clouds generally
702 form over the cooler regions of the ocean and then migrate towards the coastal land area
703 depending on favorable wind patterns. The cloud base tendencies also confirm the inland
704 advection of cool, moist air evident within the WRFDA configurations.
705 The hourly cyclic data assimilation (i) improved the model initial conditions including
706 the inversion base height significantly, (ii) subsequently reduced the overall intra-day forecast
707 biases in GHI and CSI simulations, and (iii) was especially effective in reducing GHI biases
708 during the morning and noon hours, improving the ability of grid operators to economically
709 integrate behind-the-meter rooftop solar generation. The hourly cyclic data assimilation
710 experiment depicts promising enhancements in the primary factors (discussed in the above
711 Sections) responsible for improvements in GHI forecasts in a NWP model. Additional study is
712 needed regarding other possible factors associated with marine layer stratocumulus forecasts,
713 such as improved moisture advection within the PBL and accurate estimation of inversion base
714 height at model initialization. This additional research would pave the way towards more
715 accurate cloud, and therefore GHI and CSI representation in NWP systems.
716

ACKNOWLEDGEMENTS

We are grateful to Clean Power Research for providing SolarAnywhere high resolution satellite-derived surface irradiance data, San Diego Gas & Electricity Company (SDGE) for access to their ground station irradiance measurements and the California Solar Initiative RD&D program for funding. The authors express their gratitude to Anita Zhao and Umay Akkoseoglu for formatting and editing the manuscript.

REFERENCES

Bannister, R. N., 2008a. A review of forecast error covariance statistics in atmospheric variational data assimilation. I: Characteristics and measurements of forecast error covariances. Quart. J. Roy. Meteor. Soc., 134, 1951–1970.

Bannister, R. N., 2008b. A review of forecast error covariance statistics in atmospheric variational data assimilation. II: Modelling the forecast error covariance statistics. Quart. J. Roy. Meteor. Soc., 134, 1971–1996,

Barker D. M., Huang W., Guo Y. R., Bourgeois A. J., and Xiao Q. N., 2004. A Three-Dimensional Variational Data Assimilation System for MM5: Implementation and Initial Results. Mon. Wea. Rev., 132, 897-914.

Bergthorsson P., and Doos B., 1955. Numerical weather map analysis, Tellus 7, 329-340.

Chen, T., Rossow W. B., and Zhang Y. C., 2000. Radiative effects of cloud-type variations. J. Climate 13, 264–286.

Chen F., and Dudhia J., 2001. Coupling an advanced land-surface/ hydrology model with the Penn State/ NCAR MM5 modeling system. Part I: Model description and implementation. Mon. Wea. Rev. 129, 569-585.

Chou M. D., and Suarez M. J., 1994. An efficient thermal infrared radiation parameterization for use in general circulation models. NASA Tech. Memo. 104606, 3, 85.

Courtier P., Thepaut J. N., and Hollingsworth A., 1994. A strategy for operational implementation of 4D-Var, using an incremental approach, Q. J. Roy. Meteor. Soc., 120, 1367-1387.

745 Daley, R., 1991. Atmospheric Data Analysis. Cambridge University Press, Cambridge, UK, 457
746 pp.

747 Dash S. K., Sahu D. K., Sahu S. C., 2013. Impact of AWS observations in WRF-3DVAR data
748 assimilation system: a case study on abnormal warming condition in Odisha. Nat Hazards 65,
749 767–798.

750 Ghonima, M. S., Norris J., Heus T, and Kleissl J., 2015. Reconciling and Validating the Cloud
751 Thickness and Liquid Water Path Tendencies Proposed by R. Wood and J. J. van der Dussen
752 et al. J. Atmos. Sci., 72, 2033–2040.

753 Ghonima, M. S., Heus T., Norris J., and Kleissl J., 2016. Factors controlling stratocumulus cloud
754 lifetime over coastal land. J. Atmos. Sci., 73(8), 2961-2983.

755 Ghonima, M. S., Yang, H., Kim, C. K., Heus, T., & Kleissl, J. Evaluation of WRF SCM
756 Simulations of Stratocumulus-Topped Marine and Coastal Boundary Layers and
757 Improvements to Turbulence and Entrainment Parameterizations. Journal of Advances in
758 Modeling Earth Systems. (in press)

759 Hacker, J. P., Anderson, J. L. and Pagowski, M. 2007. Improved vertical covariance estimates
760 for ensemble-Filter assimilation of near-surface observations. Mon. Wea. Rev. 135, 1021-
761 1036.

762 Hartmann, D. L., Ockert-Bell M. E., and Michelsen M. L., 1992. The effect of cloud type on
763 earth's energy balance—Global analysis. J. Climate, 5, 1281–1304.

764 Hu, X.-M., Nielsen-Gammon, J.W., Zhang, F., 2010. Evaluation of three planetary boundary
765 layer schemes in the WRF model. J. Appl. Meteorol. Climatol. 49 (9), 1831–1844.

766 Ineichen, P., Perez, R., 2002. A new airmass independent formulation for the Linke turbidity
767 coefficient. Solar Energy 73, 151–157.

768 Jankov, I., Grasso, L.D., Sengupta, M., Neiman, P.J., Zupanski, D., Zupanski, M., Lindsey, D.,
769 Hillger, D.W., Birkenheuer, D.L., Brummer,R., et al., 2011. An evaluation of five ARW–
770 WRF microphysics schemes using synthetic GOES imagery for an atmospheric river event
771 affecting the California coast. J. Hydrometeorol. 12 (4), 618–633.

772 Kain J. S., 2004. The Kain-Fritsch convective parameterization: An update. J. Appl. Meteor., 43,
773 170-181.
774 Kalnay, E., Kanamitsu, M., Kistler, R., Collins, W., Deaven, D. and co-authors. 1996. The
775 NCEP/NCAR 40-year reanalysis project. Bull. Amer. Meteor. Soc. 77, 437-471.
776 Kalnay, E. 2003. Atmospheric Modeling, Data Assimilation and Predictability. Cambridge
777 University Press, Cambridge, UK, 341 pp.
778 Kazil J., Feingold G., and Yamaguchi T., 2016. Wind speed response of marine non-precipitating
779 stratocumulus clouds over a diurnal cycle in cloud-system resolving simulations. Atmos.
780 Chem. Phys., 16, 5811-5839.
781 Lara-Fanego V., Ruiz-Arias J. A., Pozo-Vazquez D., Santos-Alamillos F.J., and Tovar-Pescador
782 J. 2012. Evaluation of the WRF model solar irradiance forecasts in Andalusia (southern
783 Spain). Solar Energy, 86(8), 2200-2217.
784 Lorenc, A. 1986. Analysis methods for numerical weather prediction. Q. J. R. Meteorol. Soc.
785 112, 1177-1194.
786 Mathiesen P., and Kleissl J., 2011. Evaluation of numerical weather prediction for intra-day solar
787 forecasting in the continental United States. Solar Energy, 85, 967-977.
788 Mathiesen P., Collier C., and Kleissl J. 2013. A high-resolution cloud assimilating numerical
789 weather prediction model for solar irradiance forecasting. Solar Energy, 92, 47-61.
790 Morrison H., Thompson G., and Tatarskii V., 2009. Impact of Cloud microphysics on the
791 development of trailing stratiform precipitation in a simulated squall line: Comparison of one
792 and two moment schemes. Mon. Wea. Rev., 137, 991-1007.
793 Nakanishi M., and Niino H., 2006. An improved Mellor-Yamada level-3 model: Its numerical
794 stability and application to a regional prediction of advection fog. Bound. Layer Meteor.,
795 119, 397-407.
796 Parrish D. F., and Derber J. C., 1992. The National Meteorological Center's spectral statistical
797 interpolation analysis system," Mon. Wea. Rev., 120, 1747-1763.
798 Perez, R., Ineichen, P., Moore, K., Kmiecik, M., Chain, C., George, R., Vignola, F., 2002. A new
799 operational model for satellite-derived irradiances: description and validation. Solar Energy
800 73, 307–317.

801 Perez, R., Lorenz, E., Pelland, S., Beauharnois, M., Van Knowe, G., Hemker, K., Heinemann,
802 D., Remund, J., Muller, S. C., Traunmuller, W., et al., 2013. Comparison of numerical
803 weather prediction solar irradiance forecasts in the US, Canada and Europe. Solar Energy,
804 94, 305–326.

805 Pu, Zhaoxia, Zhang H., and Anderson J., 2013. Ensemble Kalman filter assimilation of near-
806 surface observations over complex terrain: comparison with 3DVAR for short-range
807 forecasts. Tellus A, 65, 19620, http://dx.doi.org/10.3402/tellusa.v65i0.19620.

808 Reen B. P., and Stauffer D. R., 2010. Data Assimilation strategies in the planetary boundary
809 layer. Boundary-Layer Meteorol. 137(2), 237-269.

810 Sahu D. K., Dash S. K. and Bhan S. C., 2014. Impact of surface observations on simulation of
811 rainfall over NCR Delhi using regional background error statistics in WRF-3DVAR model.
812 Meteorol. Atmos. Phys., 125, 17-42.

813 Sahu D. K., Kim C. K., Zhong X., and Kleissl J., 2016. Assimilating in-situ observations over
814 Southern California for improved solar forecasting. Photovoltaic Specialists Conference
815 (PVSC), 2016 IEEE 43rd, 1007-1012, DOI: 10.1109/PVSC.2016.7749762.

816 Sandu I., Brenguier J. L., Thouron O., and Stevens B., 2009. How important is the vertical
817 structure for the representation of aerosol impacts on the diurnal cycle of marine
818 stratocumulus?, Atmos. Chem. Phys., 9, 4039-4052.

819 Skamarock W. C., and coauthors, 2008. A description of the advanced research WRF, version 3.
820 NCAR Tech. Note. NCAR/TN-475+STR, 113.

821 SolarAnywhere®, 2013. Web-Based Service that Provides Hourly, Satellite-Derived Solar
822 Irradiance Data Forecasted 7 Days Ahead and Archival Data Back to January 1, 1998.
823 https://www.solaranywhere.com/products/solaranywhere-data/

824 Stensrud, D., Yussouf, N., Dowell, D., and Coniglio, M. 2009. Assimilating surface data into a
825 mesoscale model ensemble: Cold pool analyses from spring 2007. Atmos. Res. 93, 207-220.

826 Stephens G. L., and Greenwald T. J., 1991. Observations of the Earth's radiation budget in
827 relation to atmospheric hydrology, Part II: Cloud effects and Cloud feedback. J. Geophys
828 Res., 96, 15325-15340.

Wang H., Huang X. Y., Sun J., Xu. D., Zhang M., Fan S., and Zhong J. 2014. Inhomogeneous Background error modeling for WRF-Var using the NMC method. J. Appl. Meteorol. Climatol. 53(10), 2287-2309.

Wilks D. 2006. Statistical methods in the atmospheric sciences, 2nd edn. Academic Press, London.

Yang H., and Kleissl J., 2016, Preprocessing WRF initial conditions for coastal stratocumulus forecasting. Solar Energy, 133, 180-193.

Zhong X., Sahu D. K., and Kleissl J. 2017. WRF inversion base height ensembles for simulating marine boundary layer stratocumulus. Solar Energy. 146, 50-64. https://doi.org/10.1016/j.solener.2017.02.021